ACS APPLIED MATERIALS & INTERFACES

www.acsami.org

Research Article

Spectroscopic Analysis of a Library of DNA Tension Probes for Mapping Cellular Forces at Fluid Interfaces

Roxanne Glazier, Pushkar Shinde, Hiroaki Ogasawara, and Khalid Salaita*

Cite This: https://dx.doi.org/10.1021/acsami.0c09774

Read Online

ACCESS | Metrics & More | Article Recommendations | Supporting Information

ABSTRACT: Oligonucleotide-based probes offer the highest spatial resolution, force sensitivity, and molecular specificity for cellular tension sensing and have been developed to measure a variety of molecular forces mediated by individual receptors in T cells, platelets, fibroblasts, B-cells, and immortalized cancer cell lines. These fluorophore−oligonucleotide conjugate probes are designed with a stem−loop structure that engages cell receptors and reversibly unfolds due to mechanical strain. With the growth of recent work bridging molecular mechanobiology and biomaterials, there is a need for a detailed spectroscopic analysis of DNA tension probes that are used for cellular imaging. In this manuscript, we conducted an analysis of 19 DNA hairpin-based tension probe variants using molecular dynamics simulations, absorption spectroscopy, and fluorescence imaging (epifluorescence and fluorescence lifetime imaging microscopy). We find that tension probes are highly sensitive to their molecular design, including donor and acceptor proximity and pairing, DNA stem−loop structure, and conjugation chemistry. We demonstrate the impact of these design features using a supported lipid bilayer model of podosome-like adhesions. Finally, we discuss the requirements for tension imaging in various biophysical contexts and offer a series of experimental recommendations, thus providing a guide for the design and application of DNA hairpin-based molecular tension probes.

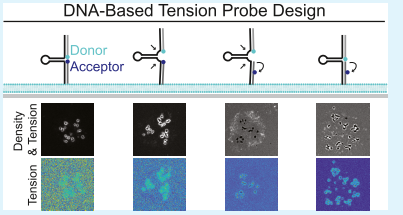

KEYWORDS: *supported lipid bilayer, FLIM, FRET, mechanotransduction, molecular probes, quenching*

INTRODUCTION

Cells transmit piconewton (pN) receptor forces to ligands in the extracellular matrix (ECM) and on the surface of adjacent cells. These forces regulate a variety of biological functions[1] including cell migration,[2] blood clotting,[3,4] and the immune response.[5,6] Understanding the precise role of mechanical forces in cell biology requires quantitative, high-resolution force spectroscopy and imaging. Bulk deformation-based approaches such as traction force microscopy and micropillar array devices are commonly used and have allowed for the quantification of cellular forces as a function of material stiffness.[7,8] A limitation inherent to these methods is their micron (μm) spatial and nanonewton (nN) mechanical resolution. Furthermore, it is challenging to apply these methods to measure forces transmitted through orthogonal ligand−receptor pairs on the same cell surface. To address these limitations, our lab developed molecular tension fluorescence microscopy (MTFM).[9] MTFM leverages DNA-based tension probes, which offer piconewton (pN) sensitivity and programmability, submicron spatial resolution, and molecular specificity.[10−12] MTFM's sensitivity and specificity have helped elucidate the role of T cell,[5,13] B cell,[14] and integrin receptor[4,15−18] mechanics in different biological processes.

In our original DNA hairpin designs, MTFM probes are comprised of a DNA hairpin (hairpin/backbone strand) flanked by a donor/acceptor pair. The probe is anchored to a surface at one terminus through an acceptor/anchor strand, while the second terminus presents a ligand (ligand/donor strand) (Scheme 1A).[15,19] The acceptor is typically a dark quencher, leading to a high signal-to-noise ratio (SNR) and facilitating probe and fluorescent protein multiplexing.[15] At rest, donor fluorescence is quenched. Upon the application of receptor forces above the $F_{1/2}$, which is defined as the equilibrium force that leads to a 50% probability of probe unfolding,[15] the hairpin opens. This causes donor/acceptor separation, yielding a ∼20−100-fold increase in donor fluorescence (Scheme 1A).[5,15] Since DNA probes are rigidly anchored to a glass substrate, probe density is fixed and the increase in fluorescence intensity is attributed to the number of mechanical events that lead to probe unfolding. In other words, the fluorescence intensity of the donor linearly reports the density of probes that are experiencing $F > F_{1/2}$, and reversible DNA-based tension probes report mechanics using a real-time, digital optical signal.[15] Because of the rotational flexibility of the probe, tensile forces rather than torsional forces extend the DNA probe from its equilibrium conformation and lead to unfolding.

Received: May 28, 2020
Accepted: October 5, 2020

Scheme 1. DNA-Based Tension Probes Report Receptor Mechanobiology[a]

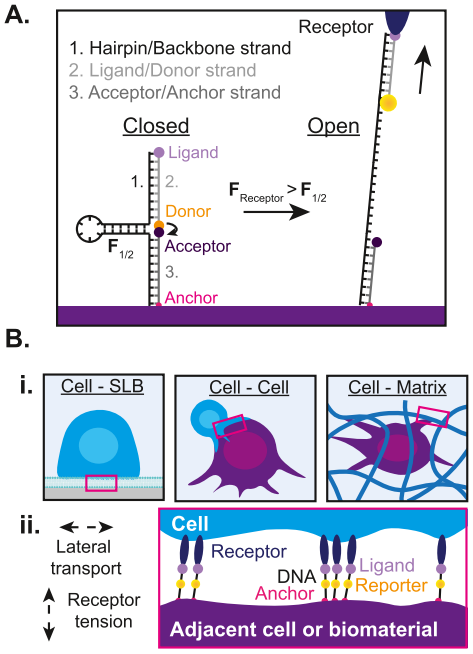

[a](A) DNA-based tension probes consist of a DNA hairpin hybridized to two arm sequences each containing a ligand or an anchor moiety. The ligand and anchor strands are labeled with a donor/acceptor pair, respectively. At rest, fluorescence is quenched. Receptor forces above the $F_{1/2}$ opening threshold lead to probe unfolding and an increase in donor fluorescence. (B) Advanced applications of molecular tension probes report receptor forces at cell-supported lipid bilayer (SLB), cell−cell, and cell−matrix interfaces (i). In these dynamic junctions, the receptors can apply tension to the DNA probes and can also spatially rearrange the probes, altering their local concentration through lateral transport (cell, SLB) or viscoelastic deformation (matrix) (ii).

While tension maps on glass have provided valuable initial insight into immune cell receptor and integrin receptor mechanosensing,[5,20,21] it is important to also perform measurements on more physiologically relevant substrates that better reflect the mechanical properties of cells and the ECM (Scheme 1Bi). Juxtacrine receptor signaling is contact-depending signaling that occurs between two cells, such as between a T cell and an antigen-presenting cell or at an epithelial cell junction. In these cell−cell junctions, which can be modeled using a supported lipid bilayer (SLB), the receptors can pull on the ligands and laterally transport them, leading to spatial reorganization and receptor clustering.[22−24] Similarly, on viscoelastic hydrogels mimicking the ECM, receptor forces cause local material deformations, which alter ligand density[25] (Scheme 1B-ii). Because of their changing ligand density, these substrates present unique challenges for tension sensing. Therefore, adapting molecular tension probes for soft materials requires additional fluorescence readouts that can decouple changes in fluorescence signal contributions from force (probe dequenching) versus clustering (probe density).

The most common method to measure forces in a system with changing probe density relies on ratiometric intensity-based imaging. This was first demonstrated by Ma et al. when mapping T cell receptor forces[26] and later was applied by Nowosad et al. when measuring B cell receptor forces on fluid membranes.[14,26] A similar approach was also used to measure cadherin tension and density in epithelial cell−cell junctions.[27] In these approaches, a third dye is incorporated into the tension probe to serve as a density reporter. One step toward measuring receptor forces in three-dimensional (3D), ratiometric DNA probes were also recently incorporated into mechanofluorescent DNA hydrogels.[28] In this case, the density and strain reporters were on separate oligonucleotide complexes and were used to quantify material strain in response to externally applied forces.

While ratiometric intensity-based measurements are advantageous in their accessibility and speed, the need for engineering three dyes in a dynamic DNA structure creates several challenges. Dyes may undergo three-way energy transfer, and the signal is subject to spectral and autofluorescent bleed-through. Ratiometric measurements are also sensitive to noise and local fluorescence artifacts. An additional challenge is that measurements require precise detector alignment and pixel registration to ensure suitable quantification.[29,30] Furthermore, ratiometric approaches occupy much of the fluorescence spectrum and are poorly suited for multiplexing, which is essential in understanding mechanotransduction and especially when one needs to tag cellular proteins in context.

To circumvent the need for a molecular density reporter, we recently developed molecular tension-fluorescence lifetime imaging microscopy (MT-FLIM), which offers a direct readout of energy-transfer states. MT-FLIM measures pN receptor tension and clustering on SLBs using DNA-based fluorescence resonance energy-transfer (FRET) probes.[16] In our original MT-FLIM report, a Cy3B/BHQ1 donor/acceptor pair was attached to a DNA hairpin-based tension probe with nine-nucleotide (nt) separation. The fluorescence lifetime, τ, was measured using time-correlated single-photon counting (TCSPC), and changes in τ uniquely reported hairpin unfolding under integrin receptor force. An empirical calibration allowed quantification of both the relative density of the probes and the percentage of the mechanically unfolded probes.

In the simplest case, a donor and acceptor pair undergoing FRET has a FRET Efficiency, E, described by

$$E = \frac{1}{1 + \left(\frac{R}{R_0}\right)^6} \quad (1)$$

R is the distance between the donor and acceptor dyes and R_0 is the Förster radius, which is a function of several variables including the dipole orientation factor, κ^2. For randomly oriented dyes, κ^2 equals 2/3. In dye-labeled oligonucleotides, this relationship often breaks down due to dye−DNA interactions and linker chemistry, which shift κ^2 away from 2/3.[31,32]

In rigidly anchored molecular tension probes, the donor/acceptor pairs are typically placed in close proximity to maximize the quenching efficiency (QE) such that only the open probes significantly contribute signal;[14,15,26,28] we termed this phenomenon as "mechanoselection".[21] However, FRET often breaks down at short distances. Nearby dyes separated by up to eight base pairs (bp) can experience short-distance fluorescence fluctuations[33] and can undergo additional quenching mechanisms such as Dexter energy transfer (DET) and static quenching. Static quenching on three-oligonucleotide complexes has been reported with up to 5 bp

https://dx.doi.org/10.1021/acsami.0c09774
ACS Appl. Mater. Interfaces XXXX, XXX, XXX−XXX

separation.[34] Therefore, although tension probes are often assumed to be FRET-quenched,[5,14,28,35] this assumption is incorrect for specific fluorophore−quencher pairs and arrangements.[36,37] Indeed, we recently reported that conventional MTFM probes employing a Cy3B donor and a BHQ1 acceptor are static-quenched.[16] While this is well established in the molecular beacon literature,[37,38] the impact of this finding on tension imaging is less explored. Static-quenched dyes form nonfluorescent ground-state complexes, which increase the SNR and improve the performance of intensity-based imaging and assays[21,39] but decrease the SNR of FLIM-based measurements, because static complexes are spectroscopically silent and do not contribute to the photons that populate the fluorescence decay histogram. Thus, to advance molecular mechanobiology through MTFM, there is a need for an empirical evaluation of the DNA-based probes to understand how fundamental photophysical processes impact imaging probe performance.

Herein, we characterized the spectral properties of a small library of DNA hairpin-based tension probes. We considered the impact of the donor/acceptor pair and positioning, as well as DNA hairpin structures (Scheme 2). We compared the absorption spectra, QE, and fluorescence lifetime of closed and open tension probes labeled with three donor/acceptor pairs: Cy3B/black hole quencher 1 (BHQ1), Alexa 488 (A488)/Cy3B, and A488/BHQ1. These three dyes, which are commonly used in DNA-based tension probes, were selected because of their imaging performance and contrasting chemical properties. Cy3B was selected as a tension reporter due to its photostability, along with its high extinction coefficient and quantum yield.[40] BHQ1 has a broad absorption and efficiently quenches fluorescence through FRET and/or static quenching in a probe-dependent manner.[38] Dye interactions are governed by a combination of van der Waals and hydrophobic interactions,[41,42] and both Cy3B and BHQ1 are hydrophobic molecules. In contrast, we selected A488 to represent the more hydrophilic dyes. A488 offers excellent imaging properties and minimally stacks with DNA.[21,43] Altogether, by considering these three donor acceptor pairs, we analyzed two probes that differed in their hydrophobicity and contained a dark acceptor and one probe with a bright acceptor, offering the potential for ratiometric readouts if desired for future applications.

Scheme 2. Summary of DNA Hairpin-Based Tension Probe Library[a]

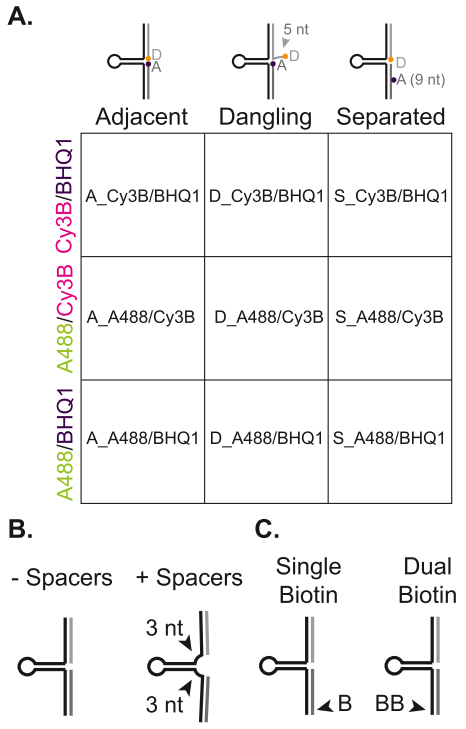

[a](A) Tension probes were evaluated with three donor/acceptor pairs and three donor/acceptor geometries. The abbreviations for each probe are provided in the chart. (B) Hairpins were tested with and without the spacers flanking the three-way junction (TWJ). Each spacer consisted of 3Ts. (C) Probes were anchored using a single or dual biotin.

Each dye pair was assessed in three geometries (Scheme 2A). In the adjacent (A) geometry, which is the conventional tension probe design,[15] the donor and acceptor fluorophores are conjugated to blunt ends of the probe's arm sequences and are separated only by the probe's three-way junction (TWJ). In the dangling (D) geometry, the donor fluorophore is conjugated to a 5 nt overhang on the ligand strand. In the separated (S) design, which was used for MT-FLIM, the acceptor is placed 9 nt away from the donor via a deoxythymidine modification.

We were also curious to understand the impact of the probe's TWJ structure. Unpaired bps increase TWJ stability.[44] Therefore, in our original MTFM probe design, the DNA hairpin's stem−loop was flanked by two spacer sequences containing 3Ts separating it from the arms.[15] These spacers were removed for MT-FLIM probes, which we hypothesized might better constrain the probes. While TWJ structure has been previously evaluated using a variety of biophysical methods,[44−46] DNA hairpin-based tension probes are nicked, which could affect their folding. Furthermore, the impact on probe performance was not clear. To better understand the impact of the TWJ on probe performance, we characterized the role of the 3T spacers in folding using molecular dynamics simulations (MDSims) and in imaging using fluorescence microscopy[16,46] (Scheme 2B).

Throughout our manuscript, we adopt a nomenclature as shown in Scheme 2A with an added + or − symbol indicating the presence or absence of the 3T spacers. Thus, a probe containing Cy3B and BHQ1 in the separated geometry with spacers would be called S_Cy3B/BHQ1+, and a probe containing Alexa 488 and BHQ1 in the dangling geometry without spacers would be called D_A488/BHQ1−.

We also investigated the impact of intra- versus intermolecular FRET in tension probe signal by tuning the dimerization of the probes using single or dual-biotin anchors (Scheme 2C). Finally, we illustrated the impact of probe design by imaging integrin receptor tension and clustering in a podosome model system using three differing probe families. We conclude with a series of recommendations to guide the use of the DNA-based tension probes in various experimental settings. This work builds upon our development of MTFM and MT-FLIM and provides important insight into the optimal design of the DNA-based tension probes to map molecular forces and receptor clustering on soft and fluid materials.

RESULTS AND DISCUSSION

Modeling of DNA Probe Structure. Prior to performing fluorescence characterization, we sought to better understand the DNA hairpin probe's TWJ structure by modeling.

https://dx.doi.org/10.1021/acsami.0c09774
ACS Appl. Mater. Interfaces XXXX, XXX, XXX−XXX

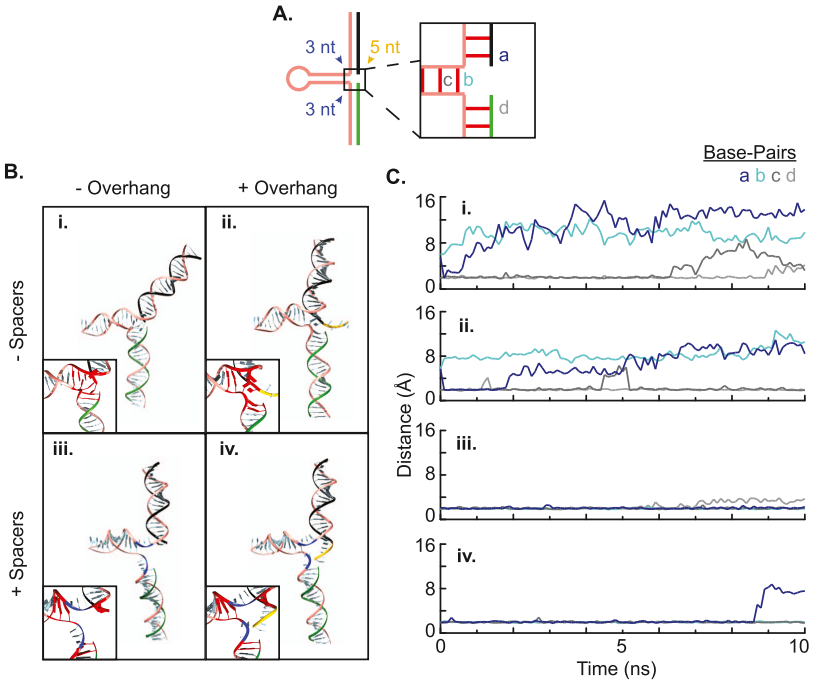

Figure 1. MD simulations predict distinct structures at hairpin probes' three-way junctions. (A) Color-coded schematic depicting the different elements of the modeled DNA hairpins. The base pairs illustrated in red are depicted in the lower-left zoom-ins in (B). The probes were modeled with and without 3 nt backbone spacers (blue) or the 5 nt overhang (yellow), which is present in the dangling (D) class of the tension probes. (B) Structured models of DNA−hairpin probes were rendered in UCSF Chimera and depict the average structures over the 10 ns simulation. The average distance between the bases was calculated throughout the simulation for each bp highlighted in red in the TWJ zoom-in. (C) Representative time traces showing the distance between indicated bp proximal to the TWJ over the course of a 10 ns simulation. BP plotted here (a−d) correspond to the indicated bp in (A) and were unstable as shown. Red bp (A, B) adjacent to (a)−(d) were stable throughout all simulations, and their distances are reported in Figure S2.

Simulations were performed on hairpins both with and without 3T spacers flanking the stem−loop structure. For each backbone, we modeled the conventional donor strand, which is used in A and S probes, as well as a donor strand containing a 5 nt overhang at the 3′ terminus, which presents the donor fluorophore in D probes (Figure 1A and Scheme 2A). Our models considered the DNA probe alone (Table S1), but these models should be interpreted with the caveat that dye−dye and dye−DNA interactions will also contribute to structure and stability. Therefore, while these data are useful in informing our understanding and highlight important design considerations, they do not fully capture the complexity of the dye-modified junctions.

To provide a coarse-grain view of the DNA probe structure, we first evaluated base pairing using the freely available NUPACK software, which computes the bp probability of hybridization but cannot provide atomistic detail (Figure S1). Fifty nM tension probes were simulated at 25 °C in 137 mM Cl^-, which approximated the conditions of probe incubation on the SLB in later experiments. The hairpin probes containing spacers were stably hybridized at all stem−loop and arm bps, both in the presence and in the absence of a 5T overhang on the donor/ligand strand. In contrast, NUPACK predicted that a fraction of the tension probes lacking spacers might experience fraying at the end of the stem−loop adjacent to the arm sequences and at the terminus of the arms. The probes containing spacers tended to be slightly more thermodynamically stable than the probes lacking spacers ($\Delta\Delta G_{\text{secondary structure}} \approx 3$ kcal/mol) (Figure S1).

We then used MDSim to gain an atomistic understanding and to further explore these findings (Figure 1). The hairpins were modeled through mutation of previously generated DNA hairpins and were simulated using the AMBER RNA force field, with 0.9% (w/v) NaCl (Figure 1A).[83] MDSim confirmed the hypothesis that the DNA probes containing spacer sequences assume a more stable conformation. We found that the hairpin geometry was highly sensitive to structural changes in the donor strand and hairpin strand (Figure 1B). The probes lacking spacers and lacking the overhang showed a more bent geometry (Figure 1B-ii). To determine which duplexes and bp would experience fraying, we quantified the distance between the hydrogen bonding groups in the bp nearest to the TWJ throughout the 10 ns simulation. We assumed that bp were H-bonding if they were within 2 Å, which is approximately equal to the average H−N bond length in a DNA duplex.[47] The probes lacking spacers experienced some stem−loop fraying, meaning that the terminal bp in the DNA hairpin exceeded H-bonding distances (Figure 1B,C-i,ii). In contrast, our data suggest that stem−loops are stable in the probes containing spacers. These probes showed some fraying of the terminal arm bp with and without a 5T overhang on the donor strand (Figure 1B,C-iii,iv). The findings were reproduced using different initial positions that placed the probe in a relatively linear conformation (Figure S2).

Absorbance Spectroscopy of Molecular Tension Probes in Solution. We next introduced dyes onto our tension probe constructs (Figures 2, S3−S5, and Table S2) and evaluated the mechanism of quenching using absorption spectroscopy. Dyes undergoing static quenching are excitonically coupled and exhibit distinct ground-state energies; this results in perturbation of the combined absorption spectra.[37,38,41] FRET and DET, however, do not impact donor and

https://dx.doi.org/10.1021/acsami.0c09774
ACS Appl. Mater. Interfaces XXXX, XXX, XXX−XXX

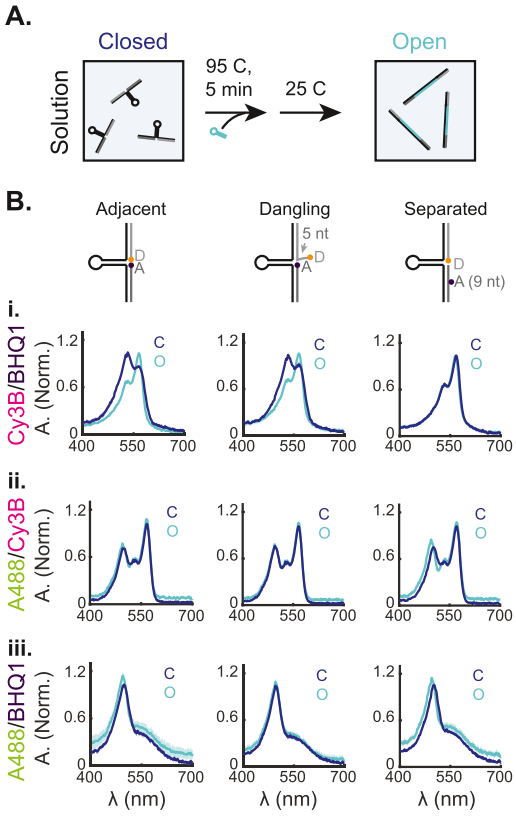

Figure 2. Absorption spectroscopy reveals ground-state and dye−DNA interactions in the molecular tension probes. (A) Tension probes were measured in solution in the closed conformation, hybridized at 95 °C with a complementary strand, and remeasured in the open conformation. (B) Absorption spectra of the closed and open tension probes with varying dye geometries for Cy3B/BHQ1 (i), A488/Cy3B (ii), and A488/BHQ1 (iii). The spectra represent the mean ± standard error of the mean (s.e.m.) from three to four experiments. The outlier spectra (baseline ± 3 median absolute deviations) were omitted. The absorption spectra for the S_Cy3B/BHQ1 probes only are reproduced with permission from ref 16. Copyright 2019 Springer Nature.

acceptor fluorophore absorption.[48] We therefore measured the absorption spectra of both closed and open tension probes (Figure 2A). First, closed probes (~2.5 μM) were annealed and concentrated to ~10 μM. Then, the absorption spectra were measured using a microvolume (Nanodrop) instrument in 4× phosphate-buffered saline (PBS). The probes were then opened by annealing with 10-fold excess of an oligonucleotide complementary to the hairpin's stem−loop sequence, concentrated, and remeasured in the open conformation (Figure 2A). For these experiments, only the tension probes lacking the backbone spacers were measured.

We first collected the absorbance spectra of the closed and open probes labeled with the donor only or the accepter only in all permutations of Scheme 2a (Figure S6; Tables S3 and S4). These data served as a control to account for dye−DNA interactions. Across the different probe designs, the absorption spectra for the probes containing Cy3B or BHQ1 alone did not display significant spectral changes between the open and closed states. In contrast, A488-containing probes in the A and S designs exhibited a 6 nm bathochromic shift in the absorption maximum ($\lambda_{max,closed}$ = 502 nm, $\lambda_{max,open}$ = 496 nm). This shift was not observed when the dye was conjugated to a 5 nt overhang (D probes), and λ_{max} remained at 495 nm for both open and closed forms. These data suggest that the small bathochromic shift in the A and S probes is due to A488's proximity to specific nucleobases within the TWJ; this proximity is removed upon opening of the hairpin.

To calculate the predicted absorbance spectra, which hold for the non-static-quenched probes, the donor and acceptor absorbance spectra were next weighted by their relative extinction coefficient, ε, and summed (Figure S7). All donor/acceptor-modified probes had overlapping open and closed spectra, except for the A488 probes without a 5 nt spacer (A and S geometries), in which, as expected, the bathochromic shift observed for the donor-only probes was maintained in the summed donor/acceptor spectra.

We next measured the absorption spectra of the donor/acceptor-labeled probes to determine which probes undergo static quenching in their closed conformation. We first discuss the Cy3B/BHQ1 probes, which displayed two major absorption peaks centered at λ_{max} = 535 and 570 nm for the A, D, and S probes in the open and in the closed states (Table S5 and Figure 2B-i). These λ_{max} values were closely matched to the absorption peaks of the Cy3B-only probes (Figure S6). Because of its broad absorption and low extinction coefficient ($\varepsilon_{BHQ1,520nm}$ is ~20% of that of ε_{Cy3B}), the BHQ1 absorption peak was not clearly resolved in these spectra (Figure S6, full width at half-maximum (FWHM) ≈ 160 nm). While the λ_{max} wavelengths did not change, A and D probe geometries displayed differing peak intensities for the open and closed states, with the 535 nm peak dominating the signal in the closed probes and the 570 nm peak most intense in the open probes. This contrasted with the S probes, which had identical open and closed probes that were very similar to the Cy3B-only probes. The spectral changes in the A and D probes suggest that the Cy3B/BHQ1 probes undergo static quenching when the chromophores are in proximity in the closed probes (A or D) but switch to FRET when these probes are opened. The absorption spectra shift of the closed probes in the D configuration (D_Cy3B/BHQ1−) suggests that a static complex formed despite the 5 nt overhang. In contrast, when Cy3B and BHQ1 are separated by 9 nt in the S geometry, the probes are quenched by through-space FRET and thus did not exhibit a change in absorption peak intensities.[16]

The A488/Cy3B probes showed three primary peaks in their absorption spectra (Figure 2B-ii; Table S5). These peaks correspond to the individual fluorophore absorption maxima. A488 primarily contributes to λ_{max} = 496 nm, while Cy3B primarily contributes to the λ_{max} = 535 and 570 nm absorption peaks (Tables S3−S5). In general, the absorbance spectra obtained for the A488/Cy3B probes were in good agreement with the calculated spectra, with minimal chromic shifts and intensity changes that deviated from the additive absorbance spectra (Figures 2B-ii and S7B). For all three dye geometries, the closed and open probe absorption spectra were similar. These data indicated that the A488/Cy3B probes do not tend to form a static-quenched complex, even when the donor and acceptor are nearby. As shown in the control experiments (Figures S6 and S7; Table S3), both A_A488/Cy3B− and S_A488/Cy3B− probes exhibited a small absorption change in the Alexa 488 peak between the open and closed states. The closed and open probe absorption spectra for D_A488/Cy3B− were identical. These changes were likely caused by a sequence- or geometry-dependent A488−oligonucleotide interaction when A488 was conjugated to the blunt end of a

https://dx.doi.org/10.1021/acsami.0c09774
ACS Appl. Mater. Interfaces XXXX, XXX, XXX−XXX

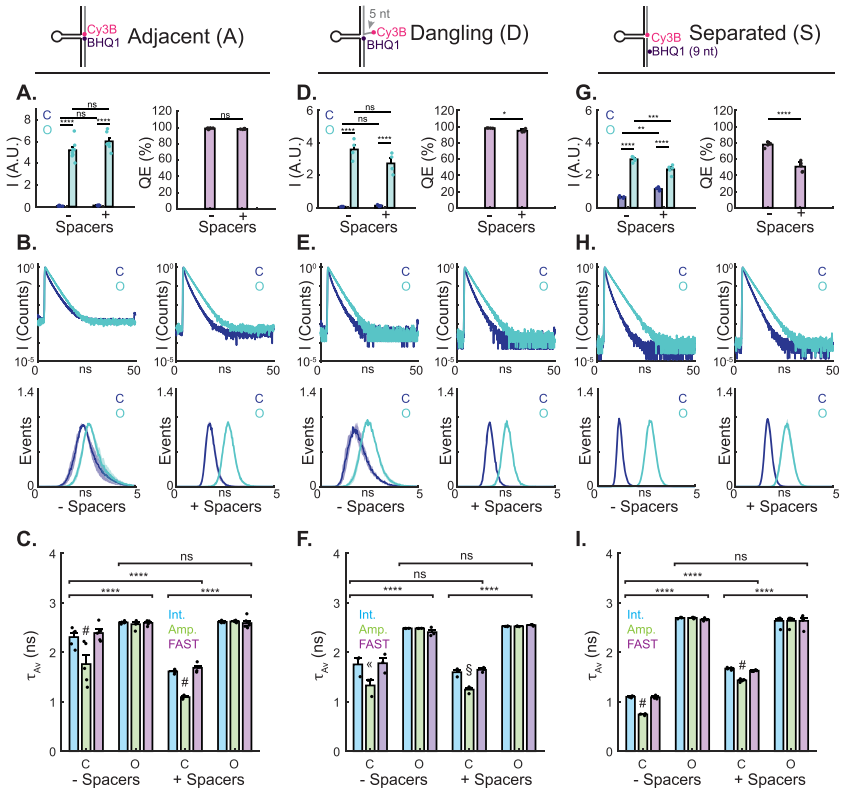

Figure 3. Fluorescence analysis of the Cy3B/BHQ1 probes on an SLB. (A, D, G) Epifluorescence intensities and QEs of the closed (C) and open (O) probes with (+) and without (−) the spacers in the adjacent, dangling, and separated geometries. The intensities were compared using a two-way grouped analysis of variance (ANOVA) followed by a multiple comparison test. QEs were compared using an unpaired two-tailed students *t*-test. (B, E, H) FLIM decay curves and FAST FLIM histograms of the closed (C) and open (O) probes. The (O) probes with (+) and without (−) the spacers in the adjacent, dangling, and separated geometries. Representative decay curves are averaged over 5 time bins. The normalized histograms represent the mean ± s.e.m. (C, F, I) Quantification of $\tau_{\text{Av Int}}$, $\tau_{\text{Av Amp}}$, and $\tau_{\text{Av FAST}}$. Statistics were performed using a three-way grouped ANOVA followed by two multiple comparison tests to look at differences across all samples or at differences between the groups but not fit methods. The experiments were repeated at least three times. *P* values are reported as ns $P > 0.05$, *, § $P < 0.05$, **, ≪ $P < 0.01$, *** $P < 0.0001$, ****, # $P < 0.0001$.

nicked duplex, which was common to A_A488/Cy3B− and S_A488/Cy3B− but not D_A488/Cy3B.

Finally, we measured the absorbance spectra of the A488/BHQ1 probes, which had a single absorption peak centered at approximately 498 nm that was accompanied by a broad shoulder corresponding to BHQ1 absorption (Figure 2B-iii; Table S5). The open and closed spectra for A488/BHQ1 followed similar trends as the A488/Cy3B probes, with a subtle chromic shift in the λ_{max} in closed versus open spectra of the A and S probes. The measured spectra were in good agreement with the calculated absorbance spectra lacking ground-state coupling (Figures 2B and S7; Tables S3−S5). These data indicated that A488 and BHQ1 do not form a static complex even when separated by only the width of the DNA hairpin duplex but rather undergo FRET or DET.

Fluorescence Imaging of the Tension Probes on SLBs. We next wanted to compare the probes' performance in fluorescence microscopy (Figures 3−5, S8, and S9; Tables S6 and S7). To evaluate probe fluorescence, we annealed the closed and open probes in solution and attached them to SLBs through biotin/streptavidin interaction. Following washing, the tension probes on SLBs were imaged using both epifluorescence and FLIM. For each probe, we used our intensity data to calculate the QE, which measures energy-transfer efficiency and can be used to determine the SNR upon probe unfolding. FLIM data provided a direct readout of probe conformation and are independent of the probe concentration during cellular imaging. The fluorescence lifetime, τ, was measured using TCSPC and is reported using three metrics. The amplitude-weighted ($\tau_{\text{Av Amp}}$) and intensity-weighted ($\tau_{\text{Av Int}}$) averages were calculated from fluorescence lifetime decay reconvolution fitting. These τ_{Av} metrics differ by lifetime component weighting; thus, they are equal for monoexponential decays but differ for multiexponential decays.[49] Typically, $\tau_{\text{Av Amp}}$ is used for FRET studies because it correlates with the steady-state fluorescence intensity. Therefore, we also used $\tau_{\text{Av Amp}}$ to calculate the efficiency of energy transfer and compared it to the intensity-derived QE (Figure S9). Note that unless otherwise stated, we use QE to refer to the intensity-derived metric. Finally, we evaluated the probes using τ_{Av} obtained by curve fitting the FAST FLIM average lifetime histogram. This metric, which we abbreviate as $\tau_{\text{Av FAST}}$, represents the mean photon arrival time and approximates $\tau_{\text{Av Int}}$. $\tau_{\text{Av FAST}}$ does not require FLIM decay fitting.

We examined all dye pairs and geometries in Scheme 2A and the impact of backbone spacer sequences (Scheme 2B). We first discuss probes employing Cy3B as a donor and next describe the A488 probes. Finally, we consider the impact of probe tethering and local concentration by imaging a subset of probes with varying biotin/streptavidin stoichiometry (Scheme 2C).

https://dx.doi.org/10.1021/acsami.0c09774
ACS Appl. Mater. Interfaces XXXX, XXX, XXX−XXX

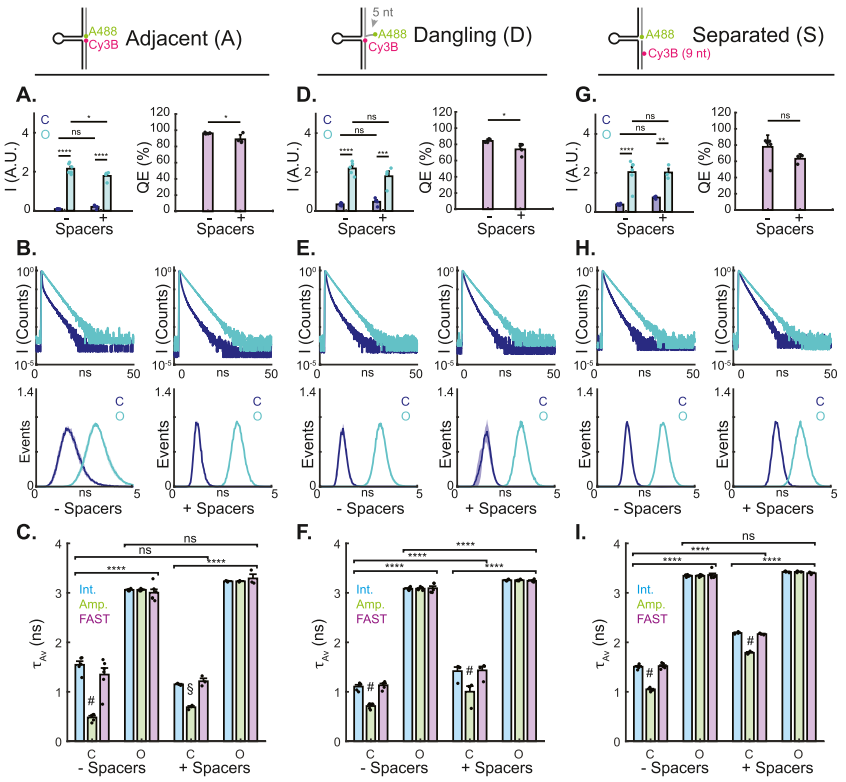

Figure 4. Fluorescence analysis of the A488/Cy3B probes on an SLB. (A, D, G) Epifluorescence intensities and QEs of the closed (C) and open (O) probes with (+) and without (−) the spacers in the adjacent, dangling, and separated geometries. The intensities were compared using a two-way grouped ANOVA followed by a multiple comparison test. QEs were compared using an unpaired two-tailed students *t*-test. (B, E, H) FLIM decay curves and FAST FLIM histograms of the closed (C) and open (O) probes. (O) probes with (+).and without (−) the spacers in the adjacent, dangling, and separated geometries. Normalized histograms represent the mean ± s.e.m. Representative decay curves are averaged over 5 time bins. Normalized histograms represent the mean ± s.e.m. (C, F, I) Quantification of $\tau_{Av\ Int}$, $\tau_{Av\ Amp}$, and $\tau_{Av\ FAST}$. Statistics were performed using a three-way grouped ANOVA followed by two multiple comparison tests to look at differences across all samples or at differences between the groups but not fit methods. The experiments were repeated at least three times. *P* values are reported as ns $P > 0.05$, *, § $P < 0.05$, **, $P < 0.01$, *** $P < 0.0001$, ****, # $P < 0.0001$.

Cy3B/BHQ1 Probes. Based on their absorption spectra, A_Cy3B/BHQ1− and D_Cy3B/BHQ1− probes were static-quenched; thus, we would not expect to see a significant change between τ_{Av} for the open and closed forms of these probes. We hypothesized that introducing the 3T spacers in the TWJ of the hairpin might cause the static-quenched state to become less populated by increasing the distance between the two dyes. This could drive the population toward FRET or DET and lead to changes in the closed fluorescence lifetime and intensity, thus altering the QE. We hypothesized that a similar perturbation to the static-quenched population may occur when the donor is separated by a 5 nt dangling end.

By measuring the fluorescence intensity of the closed and opened probes on an SLB (Figure 3 and Table S6), we found that the A_Cy3B/BHQ1−, A_Cy3B/BHQ1+, and D_Cy3B/BHQ1− probes were ∼98−99% quenched (Figure 3A,D,G). The 3T spacer incorporation in D_Cy3B/BHQ1+ reduced the QE to 95% (Figure 3D). This suggested that introducing a subtle separation between the donor and acceptor using the 3T spacers together with the 5 nt overhang partially disrupted static complex association, but that spacer sequences at the TWJ alone did not have a statistically significant effect on the QE. Nevertheless, we classify these four probes as highly quenched, because they exhibit a 20−100-fold increase in fluorescence intensity upon opening.

When these static-quenched Cy3B/BHQ1 SLBs were imaged using FLIM, we observed a reduction of τ_{Av} in the closed probes compared to the open probes (Figure 3B,C,E,F). This change was reflected in all three calculations of τ_{Av}. QE calculations resulting from FLIM data underestimated quenching compared to the intensity-derived QE (Figures S9 and S5; Tables S6 and S7), which is expected for samples containing a nonfluorescent species.[49] In this case, because the probes in the static-quenched state cannot emit photons, any signal arising from SLBs with the closed probes must be contributed by minor populations of the transiently non-static-quenched probes or impurities (Scheme 3A, *vide infra*). The probes containing 3T spacers had a shorter fluorescence lifetime compared to the probes lacking the spacers, which suggested that fewer probes formed static complexes.

As a comparison to these probes, we imaged the FRET-quenched S_Cy3B/BHQ1 probes (MT-FLIM probes[16]), which completely eliminate static quenching. As expected, closed S_Cy3B/BHQ1− were brighter than static-quenched probes (Figure 3G). These probes exhibited the shortest fluorescence lifetime of the Cy3B/BHQ1 data set; this short lifetime is due to conventional FRET quenching (Figure 3C,F,I). In contrast to the static-quenched probes, the FRET-quenched S_Cy3B/BHQ1 probes displayed a reduction in the QE and an increase in the closed fluorescence lifetime in the probes with spacers (S_Cy3B/BHQ1+) compared to the

https://dx.doi.org/10.1021/acsami.0c09774
ACS Appl. Mater. Interfaces XXXX, XXX, XXX−XXX

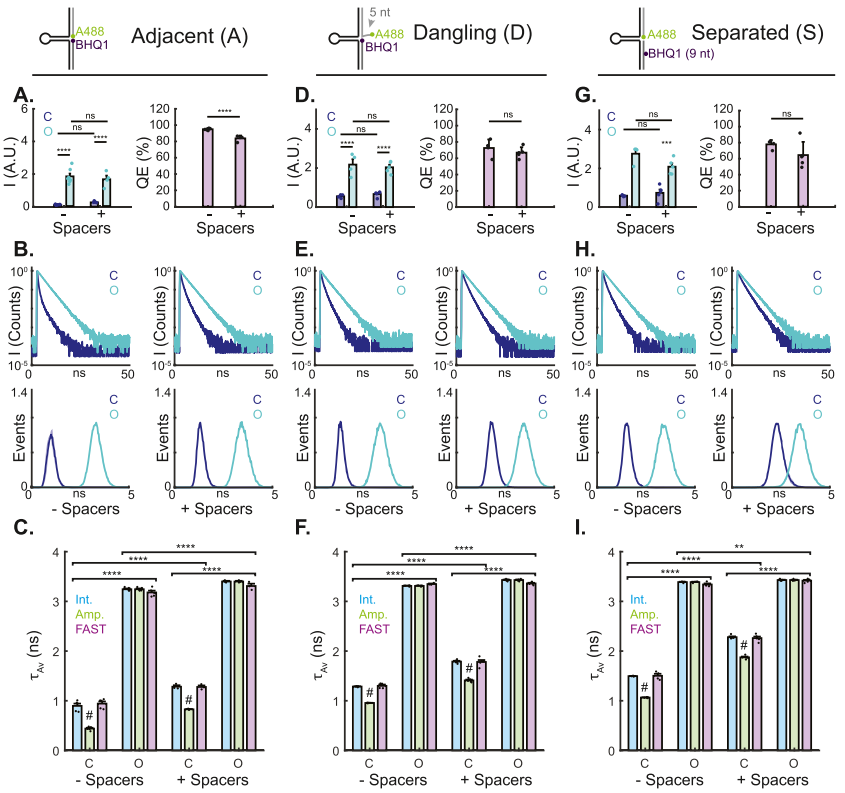

Figure 5. Fluorescence analysis of the A488/BHQ1 probes on an SLB. (A, D, G) Epifluorescence intensities and QEs of the closed (C) and open (O) probes with (+) and without (−) the spacers in the adjacent, dangling, and separated geometries. (B, E, H) FLIM decay curves and FAST FLIM histograms of closed (C) and open (O) probes. The intensities were compared using a two-way grouped ANOVA followed by a multiple comparison test. QEs were compared using an unpaired two-tailed students *t*-test. Normalized histograms represent the mean ± s.e.m. Representative decay curves are averaged over 5 time bins. Normalized histograms represent the mean ± s.e.m. (C, F, I) Quantification of $\tau_{Av\ Int}$, $\tau_{Av\ Amp}$, and $\tau_{Av\ FAST}$. Statistics were performed using a three-way grouped ANOVA followed by two multiple comparison tests to look at differences across all samples or at differences between the groups but not the fit methods. The experiments were repeated at least three times. *P* values are reported as ns $P > 0.05$, *, $P < 0.05$, **, $P < 0.01$, *** $P < 0.0001$, ****, # $P < 0.0001$.

probes without spacers (S_Cy3B/BHQ1−) (Figure 3G,H,I). These results are explained by the larger radius between the Cy3B and BHQ1 pair at rest with the addition of backbone spacer sequences.

A488 Probes. We next wanted to investigate the A488 probes with varying donor/acceptor geometries and acceptors. We hypothesized that these probes may offer an optimal combination of fluorescence intensity and lifetime sensitivity to distinguish between closed and open tension probes using both imaging modalities. Fluorescence intensity and lifetime-based tension-probe characterization were therefore repeated for the A488/Cy3B and A488/BHQ1 probes.

For all probe geometries employing A488 as a donor, introduction of the 3T spacers at the TWJ led to a general reduction in QE, although some of the probes did not show a statistical significance (Figures 4A,D,G and 5A,D,G). For the A488/Cy3B probe family, A_A488/Cy3B− offered the highest intensity-derived QE (∼95%) (Figure 4A), but these probes were subject to significant measurement challenges and uncertainties in FLIM acquisition and analysis. We found that the A_488/Cy3B− probes were extremely sensitive to acceptor photobleaching. Accordingly, we reduced laser power to reduce the photon count rate to ∼1−2% of the laser pulse rate for these samples; this reduced but likely did not eliminate the effects of bleaching. Indeed, we observed two fluorescence lifetime components in the decay (albeit with some deviation in the residuals (Figure S8). We observed a long-lifetime component, coupled with a very short fluorescence decay contributed by the quenched probes. The short component of the decay curve approached the instrument response function (IRF) (0.17 ± 0.01 ns) (Figures 4B and S8). Because of this short fluorescence lifetime component, the A_A488/Cy3B− probes had the shortest $\tau_{Av\ Amp}$. However, $\tau_{Av\ Int}$ and $\tau_{Av\ Hist}$, which estimate the average photon arrival time, were longer for A_A488/Cy3B− than for the A_A488/Cy3B+ and D_A488/Cy3B− probes (Figure 4). Because of the reduced photon count rate, the A_A488Cy3B− probes had relatively wide histogram distributions (Figure 4B). Placing the A488 on the 5T dangling end reduced the QE to 84% (from 95%) (Figure 4D) and decreased closed $\tau_{Av\ Int}$ and $\tau_{Av\ Hist}$ compared to A_A488/Cy3B− (Figure 4E,F). As expected, farther separation of the donor and acceptor in S_A488/Cy3B or through the incorporation of the 3T spacers in the backbone led to a decreased relative QE and a longer closed τ_{Av} (Figure 4G−I).

Finally, we compared quenching in the A488/BHQ1 probes, which have a dark acceptor but do not form a ground-state complex. The A488/BHQ1 probes behaved similarly to the A488/Cy3B probes but were less susceptible to acceptor photobleaching than the A_A488/Cy3B probes. Thus, the A_A488/BHQ1, D_A488/BHQ1, and S_A488/BHQ1 probes exhibited sequential increasing closed τ_{Av} and decreasing QE (Figure 5), which is the expected trend for a DET or FRET pair separated by increasing radii. For all three probe

https://dx.doi.org/10.1021/acsami.0c09774
ACS Appl. Mater. Interfaces XXXX, XXX, XXX−XXX

geometries, the introduction of the 3T backbone spacer sequences led to an increase in the $\tau_{\text{Av Closed}}$.

Probe Conjugation. Having characterized our library of tension probes using imaging, we next sought to elucidate the impact of probe conjugation on fluorescence. Given that all closed tension probes in our library exhibited multiexponential decays (Figure S8) and that $\tau_{\text{Av FAST}}$ for the S_Cy3B/BHQ1− probes was previously shown to increase the most steeply when a small number of probes were opened,[16] we hypothesized that the probes may interact through intermolecular FRET introduced as a result of the surface attachment. In this case, the donor would not only be quenched by the internal BHQ1 but would also be quenched by the dyes on the nearby probes. While FLIM is concentration-independent in dilute solutions, when conjugated to an SLB through biotin/streptavidin interaction, we hypothesized that two tension probes may be clustered onto a single streptavidin molecule. Indeed, it was previously shown that streptavidin occupancy is sensitive to the total density of biotinylated lipids and biotin mobility[50] and to the concentration of and steric hinderance imparted by biotinylated oligonucleotide probes.[51] For SLBs containing 5 mol % biotinylated lipids, the average occupancy of the streptavidin molecules was previously reported to be 1.74.[50] In our system, occupancy >1 probe per streptavidin could bring two tension probes within the FRET radius. To determine the streptavidin occupancy in our system and to test whether streptavidin-mediated probe clustering leads to intermolecular FRET, we therefore quantified the fluorescence intensity and τ for SLBs containing the DNA probes anchored with varying biotin stoichiometry.

The tension probes were anchored either using a single biotin on the 3′ terminus of the anchor strand or using a dual biotin attached to the 5′ terminus of the hairpin sequence (Figure 6A). Because SLB binding is multivalent,[50] each streptavidin presents one to two open binding sites. We therefore expected that streptavidin could bind up to two biotinylated tension probes per molecule. If the monovalent biotin anchor is replaced with a dual-biotin anchor, this number is reduced to a maximum of one tension probe per streptavidin (Figure S10). Any observed differences in the QE and τ of these samples should reflect the extent of intermolecular quenching. For these studies, we selected the S_Cy3B/BHQ1− probes for analysis, because these probes were free from ground state and dye−DNA interactions and because we previously characterized these probes on SLBs with varying biotin concentration, which showed a slight concentration dependency.[16] For the single and dual-biotin probes, we measured the fluorescence intensity and lifetime of the bilayers presenting a binary mixture of the closed and open probes, which were prepared separately and mixed in known ratios immediately prior to incubation on streptavidin-modified SLBs.

SLBs presenting probes with a dual biotin were less fluorescent than SLBs presenting single-biotin-labeled probes (Figure 6B). For example, on the 100% open surfaces, single-biotin SLBs were 56 ± 15% brighter than dual-biotin SLBs. Despite the lower intensity for the dual-biotin probes, the calculated QE was similar for the probes conjugated using a single or dual-biotin anchor. Single and dual biotin were 79 and 76% quenched, respectively, based on linear regression; these differences in QE were not statically significant (Figure 6B).

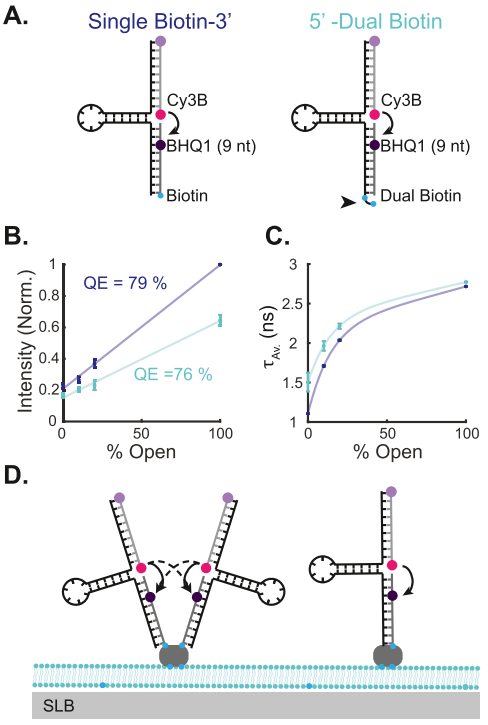

Figure 6. Streptavidin-anchored tension probes undergo intermolecular FRET. (A) Schematic of the tension probes containing a single or dual-biotin group used in this experiment. (B) Plot of the percentage of the open probes versus fluorescence intensity normalized to the single-biotin 100% open intensity. The QE for each probe was reported as the slope of the corresponding linear curve fit. (C) Percentage of the open probes versus $\tau_{\text{Av FAST}}$. (D) Streptavidin on the SLB binds 1-2 tension probes. For S_Cy3B/BHQ1- probes, probes can undergo intermolecular and/or intramolecular FRET, indicated by dashed and solid arrows, respectively. Data in (B) and (C) represent the mean ± s.e.m. of three independent experiments.

When the probes were imaged using FLIM, $\tau_{\text{Av FAST}}$ increased as a function of the percent open probes (Figure 6C). For all the surfaces tested with varying fractions of the open to closed probes, the lifetime of the mono-biotin probes was shorter than that of the dual-biotin probes. The closed probe fluorescence lifetime decay remained multiexponential even for the probes attached with a dual biotin (Figure S11).

The similar fluorescence lifetimes for SLBs containing 100% open mono- or dual-biotin probes indicate that the open probes are primarily noninteracting. If we assume that each streptavidin molecule can bind a single dual-biotin probe, then based on our 100% open intensity data, we estimate that ∼50% of streptavidin molecules are occupied with two mono-biotin tension probes (Figure 6D). The 100% closed probe lifetimes have more significant differences; this suggests a greater magnitude of intermolecular interactions, but the precise contribution of intermolecular energy transfer is more challenging to quantify. Despite the steric bulk of the DNA hairpin probes, we still find that 50% of streptavidin can bind two mono-biotin probes, which is consistent with the literature precedent.

Tension Imaging of Podosome-Like Adhesions Using FLIM. Finally, to elucidate tension probe design in the context of live-cell imaging, we imaged cellular tension signal on SLBs using six representative tension probes. For this study, we focused on the A and S probe geometries with and without the

https://dx.doi.org/10.1021/acsami.0c09774
ACS Appl. Mater. Interfaces XXXX, XXX, XXX−XXX

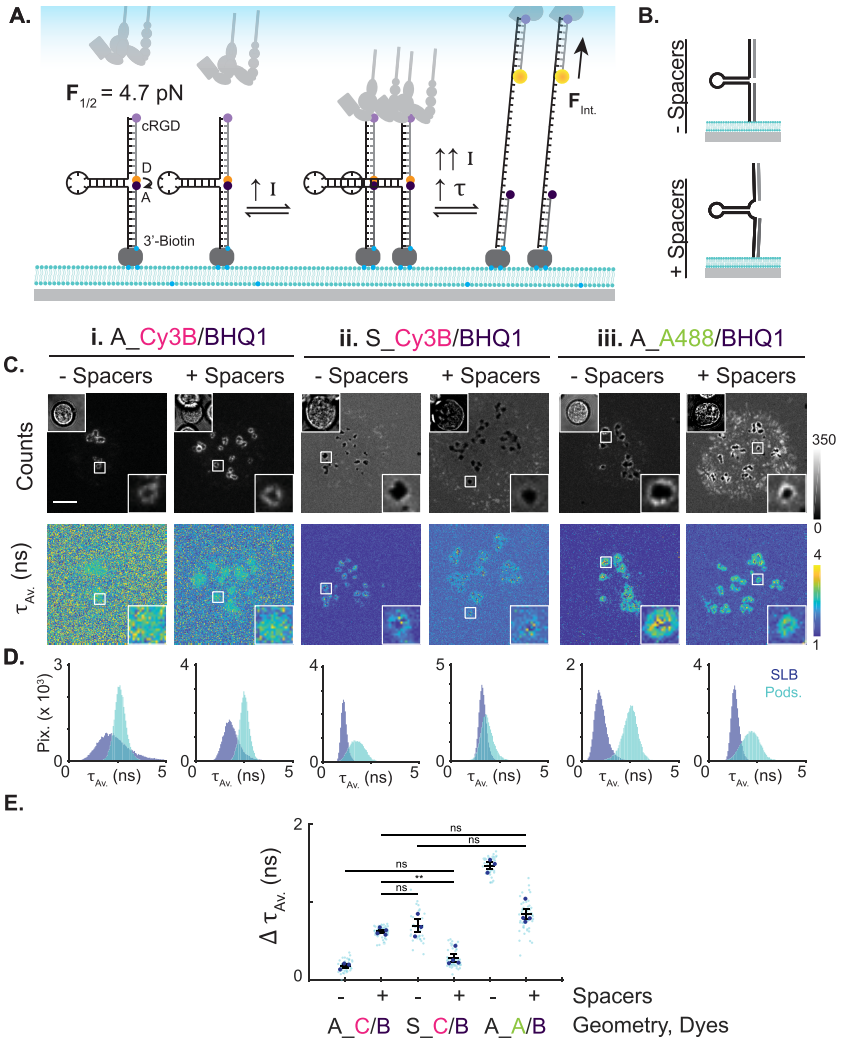

Figure 7. Tension probe design impacts the cellular readout. (A) Schematic of integrin receptor and tension probe interactions on an SLB. The unbound probes are closed and undergo quenching. Integrin receptor binding and clustering leads to an increase in density and intensity (I). Alternatively, the probes can be depleted, leading to a loss of fluorescence (not shown). Upon integrin receptor forces above $F_{1/2}$, the hairpin unfolds, causing an increase in intensity (I) and fluorescence lifetime (τ). (B) Cells were imaged on 4.7 pN tension probes containing (+) or lacking (−) spacer sequences. (C) Representative images of NIH-3T3 cells imaged on SLBs containing the indicated tension probes. Insets in the top left corners show transmitted light images. (D) Histogram analysis of the images shown above in (C). For each probe, N random pixels were selected in the SLB background, where N was the number of pixels in the podosome region. (E) Quantification of the change in $\Delta\tau_{Av}$, which is defined as the difference between $\tau_{Av\ FAST,\ Podosomes}$ and $\tau_{Av\ FAST,\ SLB}$ on the six evaluated tension probes. The small teal markers represent data points from individual cells; the large blue markers represent the mean per bioreplicate. The error bars represent the mean ± s.e.m. To compare the performance of individual tension probes, statistics were performed using a one-way ANOVA followed by a multiple comparison test. The experiments were repeated at least three times. All interactions were significant at the level of $P < 0.0001$ unless indicated with ns, $P > 0.05$, or **, $P < 0.01$. Scale bar, 5 μm.

3T backbone spacer sequences. These probes allowed us to understand the combined effects of quenching mechanism, QE, and τ in live-cell tension imaging. Specifically, A_Cy3B/BHQ1− and + were selected to demonstrate the cell imaging performance of the static-quenched probes. The S_Cy3B/BHQ1− and + probes were selected to test the impact of the 3T spacers in the FRET probes with a large closed donor−acceptor radius. Finally, A_A488/BHQ1− and + were examined, because while both probes offered a large change in τ upon opening (Figure 5), these probes differed significantly in their QE: A_A488/BHQ1− exhibits a ∼20-fold increase in fluorescence intensity upon opening, compared to A_A488/BHQ1+, which only displays a ∼6-fold increase in intensity upon unfolding.

As a model of receptor mechanobiology with dynamic ligand density, we imaged integrin receptor tensile forces in podosome-like adhesions on an SLB. Podosomes are protrusive structures that consist of a microscale actin core that physically pushes away from the cell body.[52] The podosome actin core is surrounded by an integrin adhesion ring that exerts tensile forces.[16,53,54] Within ∼1 h of spreading, fibroblasts on SLBs form multiple podosome-like adhesions, which have been previously validated and characterized using immunostaining and MT-FLIM.[16,55−57] In the model used here, integrin receptors on fibroblasts bind to cyclic-Arg-Gly-Asp (cRGD) ligands on the tension probes. The bound probes can be laterally transported, leading to a change in probe density, which is reported as a change in intensity (I) and is measured by changes in the photon count channel. When

https://dx.doi.org/10.1021/acsami.0c09774
ACS Appl. Mater. Interfaces XXXX, XXX, XXX−XXX

integrin receptors exert forces above the $F_{1/2}$ threshold, the probes mechanically unfold, leading to an increase in I that is coupled to an increase in the τ_{Av} (Figure 7A). The podosome's actin core exerts pushing forces on the SLB, which causes physical exclusion of the cRGD ligands and is indicated by a dark depletion region. Podosome pushing is accompanied by the application of pN tension in the podosome ring, leading to an increase in τ. Integrin receptors can also cluster the ligands outside of the podosome regions, leading to bright puncta (enhanced photon counts) without a measurable change in fluorescence lifetime,[16] indicating a lack of detectable mechanical tension.

For each selected geometry and donor/acceptor pair, we quantified $\Delta\tau_{Av}$, the change in fluorescence lifetime between the podosome regions and the SLB background on probes both containing and lacking the 3T backbone spacers (Figure 7B). The fluorescence lifetime per pixel was reported using the $\tau_{Av\ FAST}$. We selected this metric, because it allowed us to estimate τ_{Av} on a per-pixel basis, which is desirable to map receptor tension and clustering. Ideally, $\tau_{Av\ Amp}$ is the preferred quantification metric for FLIM-FRET, because it can provide the steady-state fluorescence lifetime and the binary distribution of open to closed probes in any given region of interest (ROI) within the sample. However, we found that the relationship between fluorescence lifetime and intensity was not equal (Figure S9), and similar discrepancies were previously reported for DNA−dye conjugates.[58,59] Moreover, because of limits in the number of photons collected due to probe brightness, detection limits, and live-cell dynamics, it is not possible to maintain high spatial resolution while curve fitting using $\tau_{Av\ Amp}$. Accordingly, we used $\tau_{Av\ FAST}$ as a suitable alternative, since it provides spatially resolved maps that estimate probe lifetimes and can be easily integrated with quantitative intensity-based thresholding workflows for cellular analysis (Figures S12−S14). Note that while the graphs in our main figures report the change in the fluorescence lifetime ($\Delta\tau_{Av\ FAST}$) in the podosome regions, for the DNA-based tension probes, the relationship between probe opening and fluorescence lifetime is not linear (Figure 6).[16] To ensure that the apparent τ values were attributed to hairpin unfolding, we imaged the cells on the control probes, which mimicked the six selected tension probes but lacked a stem−loop sequence (Figure S15A,B). The cells can bind and even mechanically pull on the RGD peptides on these control probes, but because these probes lack the hairpin motif, integrin tension cannot dequench the fluorophores.

FLIM imaging of the cells spread on the A_Cy3B/BHQ1− and + probes revealed bright rings in the photon counting channel (Figure 7C-i). The rings corresponded to the podosomes' integrin receptor adhesion rings and exhibited an increase in τ (Figure 7D,E), which is attributed to probe unfolding under force. Because A_Cy3B/BHQ1− and + probes are static-quenched and only a small population of donor dyes can fluoresce, the SLB background had very low photon counts and a high variance in τ (Figure 7C-i,D). Bright podosome rings had a narrower τ distribution, which overlapped entirely with the SLB background τ distribution. The broad range of τ values in the background included a contribution from noise and single-molecule Cy3B contamination that was persistent. When quantified on a per-cell level, a subtle shift in τ was observed in podosomes on A_Cy3B/BHQ1− compared to the SLB background outside of the cell ($\Delta\tau_{Av}$ = 0.19 ± 0.02 ns) (Figure 7E). A_Cy3B/BHQ1+ had a larger shift $\Delta\tau_{Av}$ in the podosome regions ($\Delta\tau_{Av}$ = 0.63 ± 0.02 ns) compared to the SLB background (Figure 7E). This is likely because of a reduced contribution of static quenching in the A_Cy3B/BHQ1+ probes, leading to a larger change in τ across the closed and opened probes (Figure 3A−C). In control experiments using linear probes, τ did not increase in the podosome rings, indicating that the small but significant observed changes on the A_Cy3B/BHQ1− probes are caused by force-mediated hairpin unfolding (Figure S15C−E). Interestingly, the podosomes on linear A_Cy3B/BHQ1+ probes exhibited a dim ring pattern, that had a shorter τ compared to the SLB background (Figure S15E-i). This could be attributed to entropic spring extension of the linear probes containing the spacers, which transitions the fluorophores from a static-quenched state to a through-space quenching mechanism.

FLIM-FRET images of the podosome-forming cells on S_Cy3B/BHQ1− and S_Cy3B/BHQ1+ probes (Figure 7C-ii) provided more information about the cell−SLB interaction. In contrast to the static-quenched probes, S_Cy3B/BHQ1 probes are fluorescent at rest, offering improved contrast for changes in probe density. On the S_Cy3B/BHQ1− probes, in addition to the bright rings observed on static-quenched SLBs, two additional features were visible. Within the bright podosome rings, we observed dark spots, caused by the podosome's core depletion zone. Bright receptor clusters also emerged at the cell periphery but did not exert detectable tension signal. Peripheral clusters and depletion zones were also observed on the S_Cy3B/BHQ1+ probes, but tension rings were faint. We attribute this to the competing effects of probe depletion and an only 2-fold increase in probe brightness upon opening for S_Cy3B/BHQ1+ (QE ≈ 50%, Figure 3G and Table S6). Nevertheless, on both types of surfaces, the podosome rings displayed an increase in τ compared to the SLB background (Figure 7C-ii,D,E). For the S_Cy3B/BHQ1− probes, the change in fluorescence lifetime per cell was comparable to that of the A_Cy3B/BHQ1+ probes (Figure 7E). However, podosome lifetimes were better separated from that of the SLB background because the SLB had a shorter and more narrowly distributed τ_{Av} (Figure 7E). Because of the larger dye−dye radius and lower energy-transfer efficiency for the S_Cy3B/BHQ1+ probes, podosomes on these SLBs had a smaller $\Delta\tau$. When the stem−loop sequence was replaced with a linear oligonucleotide, the podosome regions showed only a subtle increase in τ_{Av}, indicating that $\Delta\tau_{Av}$ was caused by mechanical unfolding (Figure S15C−E-ii). The change in podosome τ_{Av} on the linear S_Cy3B/BHQ1 probes was not significantly different in the presence or absence of the backbone spacers, suggesting that flexibility of these spacers under force had a minor contribution on the tension signal, which can be expected for FRET at this distance.

Finally, we imaged the podosome-forming cells on the A488/BHQ1 probes. These probes provided an example of tension signal on both highly and intermediately quenched probes with no static quenching (Figure 7C−E). We first imaged the podosome-forming cells on the A_A488/BHQ1− probes. On these probes, the photon count channel showed bright rings corresponding to the adhesion rings. Podosome depletion and receptor clustering were less obscured than on the static-quenched probes, but were still largely suppressed, due to the probe's ∼95% QE. The podosome rings had the largest $\Delta\tau_{Av}$ on the A_A488/BHQ1− probes, with little overlap in τ_{Av} between the SLB background and podosome

https://dx.doi.org/10.1021/acsami.0c09774
ACS Appl. Mater. Interfaces XXXX, XXX, XXX−XXX

ring regions (Figure 7C-E-iii). We attribute this to the $\Delta\tau_{\text{Av Closed-Open}}$ for the A_A488/BHQ1− probes (Figure 5B,C), which results from the short donor/acceptor radius and long intrinsic τ_{A488}.

With the incorporation of a spacer sequence in the A_A488/BHQ1+ probes, the fluorescence signal more closely resembled that of the cells on the S_Cy3B/BHQ1− probes, which had a moderate QE. The cells on the A_A488/BHQ1+ probes exhibited bright receptor clusters, podosome rings, and dark podosome core depletion regions. While $\Delta\tau_{\text{Av Closed-Open}}$ is smaller in A_A488/BHQ1+ compared to A_A488/BHQ1, these probes still maintained a sufficiently large dynamic range for tension mapping and quantification. Thus, these probes offered good separation in τ between the SLB background and podosome regions (Figure 7D), with $\Delta\tau_{\text{Podosome-SLB}}$ not significantly different than that observed on the S_Cy3B/BHQ1− probes (Figure 7E). Podosomes on analogous linear probes exhibited an increase in $\Delta\tau_{\text{Av Podosome-SLB}}$ that was smaller than that for hairpin probes, confirming that mechanical unfolding of the hairpin was the primary mechanism driving changes in τ (Figure S15C−E-iii).

CONCLUSIONS

Discussion of Tension Probe Fluorescence. Although several studies have focused on sm-FRET and dye−DNA interactions, fewer studies perform side-by-side spectroscopic and imaging measurements to understand the practical impact of molecular tension probe design on cellular imaging. Indeed, our lab has found that different biological systems require slightly different tension probe variants to maximize signal.[5,13,15,16] Our library here focused on DNA hairpin structure and energy transfer specifically in the context of the DNA-based MTFM probes. Interestingly, in our absorption spectroscopy data (Figures 2 and S6), we observed some dye−DNA interaction in Alexa 488 probes lacking a 5T overhang. Since A488 has a low anisotropy on DNA,[21,43] we hypothesize that interaction is caused by proximal guanosine quenching, which can alter absorbance in some cases.[60]

The three donor/acceptor spatial arrangements (A, D, and S) offered sequential perturbation of tension probe geometry. All separated tension probes were FRET-quenched. When the donor and acceptor dyes were separated only by the width of the DNA hairpin duplex in the adjacent geometry, the Cy3B/BHQ1 probes were static-quenched and the A488 probes underwent dynamic quenching. We previously reported that A_Cy3B/BHQ1+ probes are static-quenched,[16] and as expected, this observation was maintained for the A_Cy3B/BHQ1− probes, which further reduce the donor/acceptor radius. Marras and colleagues reported that a 5 nt overhang at the end of a duplex maximized FRET while significantly decreasing static quenching between a donor−acceptor pair.[38] We had therefore hypothesized that separation of the Cy3B and BHQ1 through a short overhang may reduce dye interactions. However, our results indicated that the 5 nt overhang was insufficient to remove ground-state interactions in our D_Cy3B/BHQ1− probes. Additionally, the MD simulations (Figure 1B) also showed that the addition of the 5 nt overhang places the terminal base in a position that would be favorable for contact quenching interactions to occur. We measured 98−99% QE in our static-quenched probes, which is comparable to the literature report of 97% quenching in the static-quenched Cy3/BHQ1 probes.[38] While S_A488/Cy3B and S_A488/BHQ1 probes are FRET-quenched, we cannot rule out the possibility that A and D probes may undergo a combination of FRET and DET, an additional mechanism of dynamic quenching that occurs at short distances (contact-mediated or through-space).[48] FRET and DET are challenging to discriminate,[36,48] and our methods were not able to resolve these two mechanisms.

Although our absorbance spectroscopy data did not support a model of A488 static quenching in the tension probes, there is literature precedent showing static quenching of this dye. In the most directly comparable report, A488 and BHQ1 were conjugated to the blunt end of a DNA duplex and showed changes in their absorption spectra that were consistent with static quenching.[38] Interestingly, the reported QE matched that of our A_A488/BHQ1− probes (96 ± 1 versus 95%[38]). We attribute the difference in the quenching mechanism here to the precise nanoscale arrangement of dyes conjugated to a single blunt end versus two blunt ends facing each other at a TWJ. Protein folding-dependent static quenching and FRET have also been reported to occur between A488 and specific amino acids,[61] and most recently, interactions between A488 and BHQ3 were suggested as the likely mechanism driving accelerated click reactions and quenching in newly developed FAST probes for multiplexed fluorescence imaging.[39] We suspect that in our system, A488 static complex formation may have been inhibited by A488's direct conjugation and confinement to the 5′ end of the donor/ligand strand. In contrast, Cy3B was conjugated using an amino modifier, which contains a longer linker that could promote Cy3B/BHQ1 hydrophobic interaction (Figure S3).

The interpretation of our static-quenched FLIM data is counterintuitive. Static-quenched samples do not typically display a change in fluorescence lifetime compared to the donor only sample, because only dequenched free dyes contribute to the fluorescence decay. However, we observed a slight decrease in the fluorescence lifetime of the static -quenched samples. This observation is especially unusual because probe anchoring to the SLB requires hybridization to the quencher-modified strand and hence each DNA-conjugated fluorophore should be accompanied by a quencher.

To understand these results, we consider the ensemble of all Cy3B molecules that contribute to an image. At any given instant, an individual probe can undergo either static or dynamic quenching, but across the ensemble there is a mixture of static, dynamic, and dequenched dyes. This is explained by thermal fluctuations of the DNA TWJ and by hydrophobic interactions of the free dye with the membrane (Scheme 3A). Although the majority of closed probes are folded, quenched, and spectroscopically silent, a small fraction of probes will thermally breathe and generate fluorescence.[62] When static-quenched complexes breathe, either due to DNA fluctuations at the TWJ or due to the fluorophore−quencher intrinsic off rate, the Cy3B and BHQ1 switch to FRET or DET, leading to the contribution of short fluorescence lifetime photons. During hairpin breathing, the fluorophore and quencher are separated and contribute long-lifetime photons. A second contribution to long-lifetime impurities is due to a small amount of free Cy3B in the sample, which partitions into the SLB[63] and is not removed by washing. Finally, when working with low photon counts, noise has a greater contribution in the measurement and may contribute to long-lifetime events. Although the dequenched probes and Cy3B impurities are relatively rare, these fluorophores have a high quantum yield and hence dominate the fluorescence decay histogram. Therefore, the

https://dx.doi.org/10.1021/acsami.0c09774
ACS Appl. Mater. Interfaces XXXX, XXX, XXX−XXX

Scheme 3. Interpretation and Implementation of the DNA-Based Tension Probes[a]

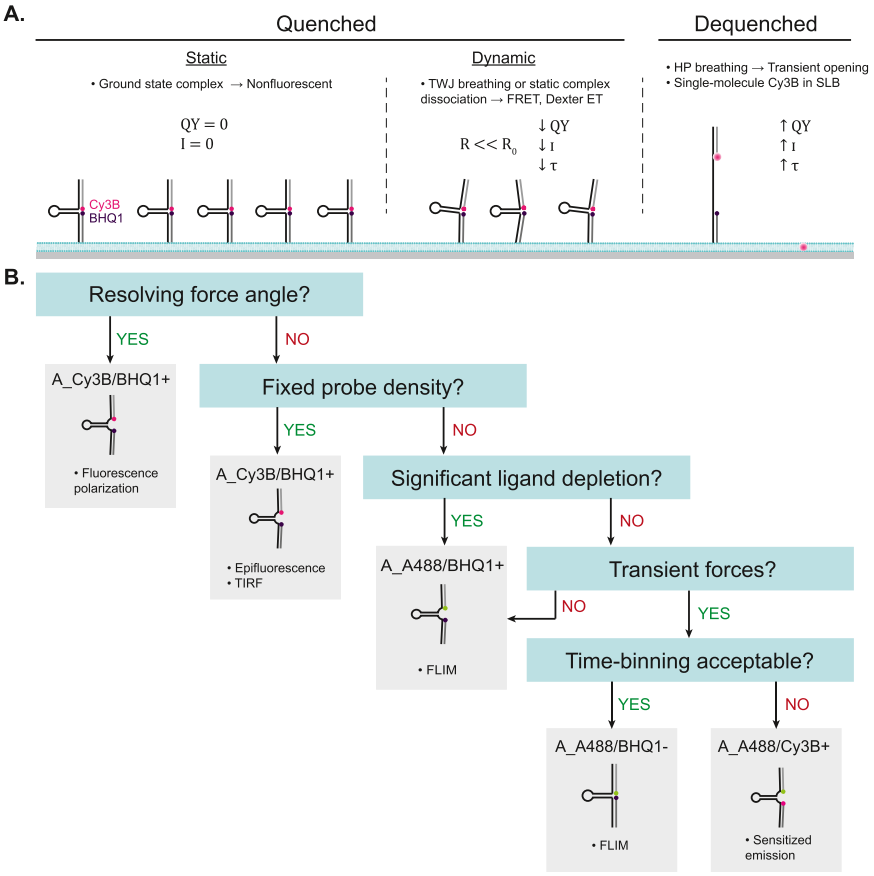

[a](A) Graphical summary illustrating probe and fluorophore states with their associated fluorescence signals. While most probes are nonfluorescent, a small subset of the Cy3B molecules are not static-quenched and emit photons with short or long lifetimes. The arrows in the dynamic quenched and dequenched panels are relative to each other but not to the static-quenched population, which does not fluoresce. (B) Decision tree indicating the best choice DNA probe and imaging modality for various cellular imaging scenarios.

~0.2−0.9 ns change in lifetime upon opening the hairpin is primarily due to photons collected from transient disassembly of the ground-state complex. This is in agreement with Sillen and Engelborghs, who argue that the average fluorescence lifetime can change in a heterogeneous population with partial static quenching.[49]

We were not able to identify imaging parameters that allowed the precise determination of A_A488/Cy3B−'s fluorescence lifetime. We attribute this challenge to the combination of the probe's high QE (96 ± 1%) combined with Cy3B's photostability. While Cy3B is known and selected for its good photostability,[40] the dye tended to bleach during probe FLIM. Acceptor photobleaching was minimized by manually attenuating the laser, but attenuation was achieved at the cost of photon counts, leading to a broad histogram distribution. Furthermore, defining the threshold was not clear, and our decay fits suggest the presence of a long-lived species, which would be expected if Cy3B were bleached. This effect was alleviated when the Cy3B was separated from the A488 donor such that the probes had a moderate QE (<90%) and a higher QY. Despite the even higher QE, we did not tend to observe these effects when A488 was paired with a BHQ1 quencher in the A_A488/BHQ1 probes. On SLBs containing primarily static-quenched probes, both Cy3B and BHQ1 photobleaching might be expected at laser powers sufficient to generate high photon fluxes. With our laser system, however, we did not reach these limits.

Across our samples, we tended to observe a discrepancy between FLIM and the intensity-based results when comparing energy-transfer efficiency in the tension probes. Even for our FRET probes (S geometry and A488 probes), the QE calculated using fluorescence intensity did not agree with the QE calculated using the $\tau_{\text{Av Amp}}$ (Tables S6 and S7; Figure S9). These differences between intensity-based and lifetime-derived energy-transfer efficiencies could arise from uncertainty in $\tau_{\text{Av Amp}}$,[64] nonradiative contributions to energy transfer,[58] or inconsistencies between the timescale of probe dynamics and the fluorescence lifetime.[65] Given the complexity of these macromolecular probes, we still advise probe calibration and controls to ensure a linear relationship between $\tau_{\text{Av Amp}}$ and the percentage of the open probes even in the cases where the intensity- and lifetime-derived QEs match.

Interpretation of Tension Probe Structural Variations. Our data indicate that tension probe performance is extremely sensitive to perturbations of the TWJ. The introduction of the spacers or an overhang significantly alters $\tau_{\text{Av Closed}}$, thus impacting the dynamic range of the readout and the ability to resolve molecular tension, clustering, and depletion. Because the probe's $F_{1/2}$ threshold is set by the DNA hairpin's length and guanine−cytosine (GC) content, these perturbations may also affect mechanics and should be

https://dx.doi.org/10.1021/acsami.0c09774
ACS Appl. Mater. Interfaces XXXX, XXX, XXX−XXX

closely considered. For the scope of this paper, we modeled tension probes lacking dye molecules. These data are somewhat limited in their interpretation, because some dyes stack against nucleobases and are known to change the duplex stability and its melting temperature.[31,38,66] Nevertheless, our modeling results highlight essential structural features and questions to be considered in tension probe design.

Welch and colleagues argued that it was physically impossible for a TWJ to undergo helical stacking without ruptured base pairing.[46] Our data suggest that a nicked duplex alone does not relieve this junctional stress, and we found that the probes lacking the spacers between the stem−loop and arms at the TWJ assume a bent, "Y" shape. The tension probes were more stable with the incorporation of the spacer sequences flanking the DNA hairpin, and the probes lacking spacers may experience some peeling of the terminal bp in the stem−loop (Figures 1, S1, and S2). This is consistent with prior literature reports that unpaired bases increase TWJ stability.[44,46] Furthermore, the near helical stacking we observed with the addition of the spacers or a 5T overhang was similar to Welch and colleagues' report that unpaired bases at the TWJ lead to a more open junction, which undergoes full helical stacking in the presence of metal ions.[46]

We argue that the practical impact of junctional changes in stability is minor. In other words, we argue that terminal bp fraying in the probes lacking the spacers will cause a relatively small change in the mechanical precision of the assay. Using an energy landscape model, Woodside et al. found that the DNA hairpins consist of a heterogeneous population, with a fraction of the hairpins experiencing stem−loop fraying. This leads to a 1−2 nm overestimation of the hairpin's opening distance in the calculation of the hairpin's ΔG_{Unfold}, which slightly shifts the energy landscape and the slope of the transition from the closed to the open state. Our modeling did not capture this fraying behavior in probes containing spacer sequences but suggests that probes lacking spacers are strongly driven toward the frayed state. The frayed probes would have 1−2 bps fewer in the stem. For the DNA probes in 1× PBS, we calculate a 1.3 pN change in $F_{1/2}$ for populations that are completely unfrayed versus completely frayed at the 2 terminal bp (Table S8). In reality, one can assume a population that is dynamically exploring these states, with the probes containing the spacers favoring the unfrayed state and the probes lacking the spacers favoring the frayed state. While the DNA hairpins have a very sharp transition,[12,15] given the discrepancies that are observed between estimated and experimentally measured $F_{1/2}$ thresholds, which range from 4.7 to 7.8 pN for this probe depending on buffer conditions,[12,15,21] this difference in mechanical stability is small. Based on the literature precedent,[38] it is likely that donor/acceptor interactions, and particularly those that result in static quenching, will stabilize the probe in the closed state. This will likely modulate the effective $F_{1/2}$ in a dye-dependent manner. Notably, while we observed changes in the quality of cell images employing various donor/acceptor pairs in the presence or absence of the spacer sequences, we did not observe changes in the regions of cellular signal that displayed probe opening, suggesting that any difference in $F_{1/2}$ was not biologically significant.

Recommendations for Cellular Imaging. Optimal tension probe design balances probe structural stability and QE with the SNR and time-resolution requirements required by the biological system and the imaging modality. Our newly characterized tension probe library reveals the nuances of probe variants, allowing for more informed probe design and implementation to meet these criteria. Here, we analyze and summarize the application of specific DNA probes for tension imaging and provide a flow chart to summarize important decisions in probe selection (Scheme 3B). For a broader and more extensive discussion on FRET imaging strategies, probe design, and troubleshooting, we refer the reader to the recent review by Algar and colleagues.[36]

In intensity-based imaging on rigid substrates, tension is indicated by an increase in brightness. Therefore, the best probes are static-quenched probes, which maximize the QE. In FLIM, tension is indicated by an increase in τ_{Av}, and probe contrast is derived from $\Delta\tau_{\text{Av Closed-Open}}$. It is desirable to have a large $\Delta\tau_{\text{Av Closed-Open}}$, but this must be achieved while maintaining the ability to robustly report both $\tau_{\text{Av Closed}}$ and $\tau_{\text{Av Open}}$. The closed probes should be sufficiently bright and photostable to image and should decay with a fluorescence lifetime that is longer than the IRF. In FLIM, detector saturation occurs when sequential photons arrive faster than the electronic dead time. This leads to the pile-up effect, in which the fluorescence lifetime is underestimated due photon omission. Avoiding pile-up requires that illumination intensity be attenuated to accommodate the brightest regions. Therefore, for FLIM it is advantageous to work in systems with more uniform brightness such that the regions with the closed probes can still be clearly imaged. Altogether, we argue that the best FLIM tension probes are FRET probes with a moderate QE, which balance the need for maximal $\Delta\tau_{\text{Closed-Open}}$ with the requirements for pixel brightness.

With some exceptions (vide infra), we generally recommend probes in the adjacent geometry that contain spacer sequences. In principle, the dangling geometry can be used to modulate energy transfer, but in practice, we found that these probes produced mixed quenching responses and were structurally more complex than probes lacking this overhang. Spacer sequences flanking the hairpin are desirable for two main reasons. First, the spacers slightly increase probe stability by reducing crowding around the TWJ. Second, spacers may offer additional benefits when tuning the $F_{1/2}$ to quantify receptor forces exerted by the cells. The $F_{1/2}$ threshold is set by the stem−loop sequence length and its GC content. GC-rich regions are known to quench fluorescence,[67,68] and a longer stem−loop will further separate dyes in open probes, which could affect the QE. The spacer sequences can serve as a buffer to minimize potential photophysical coupling between the nucleic acids of the probe and the organic dyes and to maximize the radius between the donor and acceptor in open probes regardless of stem−loop length.

For intensity-based imaging on glass, we generally recommend the A_Cy3B/BHQ+ probes, which provide the best SNR and stability. Using epifluorescence, we did not detect a significant difference in QE between A_Cy3B/BHQ1+ and A_Cy3B/BHQ1−, and while it is possible that with optimized gain settings the QE of these probes may be distinguishable, both probes offer excellent intensity contrast (Figure 3). The A_Cy3B/BHQ1− probes were previously applied for molecular force microscopy of podosome-like adhesions,[16] which leverages fluorescence polarization imaging and cyanine dye base stacking to deduce the force probe orientation. Our data here suggest that a fraction of these probes may experience 1−2 bp arm fraying, which could slightly dampen the anisotropy signal.[21] While favorable cyanine dye base stacking[31] may help overcome this effect,

https://dx.doi.org/10.1021/acsami.0c09774
ACS Appl. Mater. Interfaces XXXX, XXX, XXX−XXX

the incorporation of the spacer sequences can ensure maximum duplex stability for these experiments.

For FLIM-FRET measurements, our previously reported MT-FLIM probes (S_Cy3B/BHQ1−) provided a suitable option to image receptor clustering and tension, and A_A488/BHQ1 probes introduced here offer enhanced lifetime contrast, because of the contrast imparted by A488's long intrinsic lifetime. For samples such as the podosome model applied here, it is desirable to maximize both positive and negative SNR while maximizing lifetime sensitivity. For these cases, S_Cy3B/BHQ1− and A_A488/BHQ1+ probes offer the best imaging features. Because of the increased stability of the hairpins containing spacers, we would therefore recommend the A_A488/BHQ1+ probes as an improved FLIM-FRET probe for imaging podosome forces. The A_A488/BHQ1+ probes provide a higher SNR when comparing the clusters to the SLB background, because the higher QE of A_A488/BHQ1− dampens the signal from the receptor clusters in the absence of tension. This is particularly important to consider for systems in which receptor translocation and microclustering plays a critical role, such as the study of immune receptors.[69]

There are some cases in which the benefits of the probes lacking the spacers would outweigh the advantages of spacer incorporation. When visualizing weak or transient forces, such as the forces applied by the PD-1 receptor,[5,13] it may be advantageous to work with the more highly quenched A488/BHQ1− probes. These probes may be better suited to detecting rare forces, because nearly all photons are contributed by the mechanically opened probes and because they have a very large $\Delta\tau_{\text{Av Closed-Open}}$. The highly quenched A_A488/BHQ1− probes may also be advantageous for imaging forces applied to DNA-loaded hydrogels, in which volumetric tension probes may contribute to high background. Finally, for cells with significant autofluorescence, the original MT-FLIM probes (S_Cy3B/BHQ1−) may perform the best.

The major advantage to the A488/Cy3B probes is their potential for side-by-side intensity and FLIM-based measurements (Scheme 3B). Although FLIM-FRET is the gold standard for reporting energy transfer, intensity-based imaging is desirable when the biological system is too dynamic to perform time binning on the second-to-minute timescale. Of the current library, the A_A488/Cy3B+ probes would likely be best suited for this application. Intensity-based FRET imaging can be performed ratiometrically or using sensitized emission, which may provide a quantitative advantage by eliminating the contributions of cellular autofluorescence and evanescent field interference patterns observed in total internal reflection fluorescence microscopy.

Summary of Limitations and Advances. Our work is subject to a few caveats. We expect that the general conclusions and trends in our manuscript to be robust, but the precise fluorescence intensities and lifetimes of the dyes will likely be influenced by buffer conditions. The fluorescence lifetime of many dyes is sensitive to pH, ionic strength, and polarity,[70] and recently, quenching was shown to increase in more polar solvents.[71] Similarly, buffer conditions are known to influence DNA secondary structure, which could affect helical stacking at the TWJ[46] and may also impact the $F_{1/2}$.[12,2] While FLIM is largely insensitive to changes in concentration, intensity data is subject to DNA impurities such as degradation. On the other hand, FLIM data is more sensitive to impurities caused by trace amounts of free dye in the sample. Note that the $F_{1/2}$ parameter describes the equilibrium force that leads to a 50% unfolding probability. Highly transient forces (~μs to ms duration) require greater magnitudes of tension to drive hairpin unfolding. Hence, the receptor force values reported here represent a lower bound measurement of mechanical events. Tuning the $F_{1/2}$ may alter probe breathing dynamics, which could modulate the lifetime and intensity of the resting probes. This should be considered when designing new probes. Nearby dyes can undergo dye−dye interactions in the absence of static quenching. We did not explicitly test these effects in our system, but they should be carefully considered if transitioning from ensemble FRET measurements to tension−sm-FRET experiments.[33,72] As faster FLIM electronics become more widely available and the pile-up effect becomes a less important factor in FLIM, probe selection may be reconsidered. Thus, probe selection should be catered not only to the specific cell biology question but also to the instrument on hand.

Overall, our work highlights the significant impact of photophysics and nanoscale design on the DNA-based tension probes. While previous works have provided a more quantitative framework of energy transfer and TWJ structure in oligonucleotides on the single-molecule level, our results bridge the gap from single-molecule analysis to cellular and molecular imaging. Our data offer important insight for the future development and application of the tension probes to image receptor tension on soft materials and fluid interfaces. This work is broadly applicable to FRET sensor design and may be useful in the optimization of nucleic acid-based probes for computing and light harvesting.[73−75]

EXPERIMENTAL SECTION

Probe Synthesis and Purification. The oligonucleotides (Table S1) were custom-synthesized by Integrated DNA Technologies or Biosearch Technologies (BHQ1-modified oligonucleotides). Synthesis and purification were performed, as previously described (Figure S4).[15,16] One hundred micrograms cyclo [Arg-Gly-Asp-D-Phe-Lys(PEG-PEG)] (PCI-3696-PI, Peptides International) were reacted for 1 h with NHS-azide (88902, Thermo-Fisher Scientific) in 10 μL of dimethyl sulfoxide (MX1457-7, Millipore-Sigma). The reaction was performed in a bath sonicator and was purified using reverse-phase high-performance liquid chromatography (HPLC) on a Grace Alltech C18 column (0.75 mL/min flow rate; solvent A: Nanopure water + 0.05% trifluoracetic acid (TFA), solvent B: acetonitrile (BDH83639.400, VWR) + 0.05% TFA; starting condition 90% A + 10% B, 1%/min gradient B). To generate cRGD ligand strands, the alkyne-modified oligonucleotides were conjugated to the purified cRGD-azide performed with 10 mM sodium ascorbate, 0.4 mM copper sulfate, and 2 mM tris(3-hydroxypropyltriazolylmethyl)-amine (THPTA) (1010, Click Chemistry Tools) under a N_2 atmosphere for ~1 h. The amine-labeled oligonucleotides were conjugated to Cy3B-NHS ester (PA631000, GE Healthcare) in a 10 μL reaction containing 10% 10× PBS, 0.1 M sodium bicarbonate, and ~8× excess dye prior to initial purification on a P2 size-exclusion gel. The peptide and dye-labeled oligonucleotides were purified using HPLC on an Agilent Advanced oligo column (0.5 mL/min flow rate; solvent A: 0.1 M triethylammonium acetate (TEAA), solvent B: acetonitrile; starting condition: 90% A + 10% B, 1%/min gradient B). The Alexa 488-labeled oligonucleotides were purchased prelabeled. The HPLC products were dried in an Eppendorf Vacufuge Plus and were validated using mass spectrometry. The labeled oligonucleotides with significant excess dye were repurified using HPLC or Amicon filtration (3 kDA cutoff).

Mass Spectrometry. The molecular weight of the modified oligonucleotides was evaluated with an electron spray ionization (ESI) method using a Thermo Fisher Scientific Orbitrap, which was

https://dx.doi.org/10.1021/acsami.0c09774
ACS Appl. Mater. Interfaces XXXX, XXX, XXX−XXX

equipped with an Offline PicoTip Emitters (New Objective) (Figure S5 and Table S2). Then, the deconvolution of the ESI-MS spectrum (m/z), was analyzed with Thermo BioPharma Finder 3.2 (Thermo Scientific), was conducted to obtain averaged molecular weight of the oligonucleotides.

First, we obtained the ESI mass spectrum (negative mode). The sample oligonucleotides were injected through EconoTips emitters (New Objective) using 1−2 μM of oligos in an aqueous solution of 40 mM $(NH_4)_2CO_3$. Next, we deconvolved the obtained ESI-MS spectrum using Thermo BioPharma Finder 3.2 using Intact Protein Analysis, with the "Default SW Xtract" method. The Average Mass was the obtained molecular weight of the oligonucleotides, which averages the isotopic distribution mainly caused by ^{12}C (∼99%) and ^{13}C (∼1%). For some oligonucleotides, we observed two peaks, with the second peak corresponding to the oligonucleotide having exchanged its proton with the ammonium or sodium ions from the buffer solution or an ion source. In this case, the mass closer to the expected value was reported.

Probe Hybridization. To assemble the tension probes, DNA in 1× PBS was hybridized by heating to 90 °C for 5 min followed by cooling at 25 °C for 25 min. Hybridization was performed in a 0.2 mL Thermowell tube. For surface experiments, the donor strand was added in 10% excess. To unfold the tension probes, the complementary strand was added at 10× excess. For absorption spectroscopy, which was performed in solution, the BHQ1 samples lacked biotin. For SLB characterization, the donor strands did not contain ligands.

Supported Lipid Bilayer Formation and Functionalization. Small unilamellar vesicles (SUVs) were prepared by mixing 1,2-dioleoyl-*sn*-glycero-3-phosphocholine (DOPC) (850375C, Avanti Polar Lipids) and 1,2-dioleoyl-*sn*-glycero-3-phosphoethanolamine-*N*-(biotinyl) (Biotinyl Cap PE) (870282C, Avanti Polar Lipids) in known ratios in chloroform. SLB characterization was performed with 0.1 mol % biotinylated lipids, except for the A_Cy3B/BHQ1 probes, which were characterized using 0.2 mol % biotinylated lipids in the SLB. Cellular imaging was performed with 0.2 mol % biotinylated lipids. Chloroform was removed using rotary evaporation followed by drying under ultra-high-purity N_2. The lipids were resuspended in Nanopure water (2 mg/mL), sonicated, and freeze-thawed (three cycles). The liposomes were extruded 10× through a 0.08 or 0.2 μm filter and drain disk. To prepare SLBs using SUVs, uncoated glass-bottom 96-well plates (265300, Nunc) were base-etched for ∼1 h in ∼2.6 M NaOH and were washed with excess nanopure water and 1× PBS. One hundred microlitres of 0.5 mg/mL liposomes in PBS was added for ∼10 min to form an SLB. SLBs were washed with excess water and PBS and were stored for up to 24 h in water at 4 °C. SLBs were passivated with 0.01% bovine serum albumin, fraction V (10 735 078 001, Roche Diagnostics GmbH) prior to incubation with ∼180 nM streptavidin (SA101, Millipore-Sigma) for at least 45 min. SLBs were washed with excess 1× PBS and incubated in ∼30−45 nM DNA for at least 45 min prior to imaging. Imaging was conducted in 1× PBS (cell-free assays) or in Hanks Balanced Salts (cell assays, H1387, Sigma-Alrich).

Modeling. All hairpins probes were modeled in YASARA[76] and visualized in Chimera.[77] Following cell neutralization,[78] YASARA simulation was performed atomistically for 10 ns under an isothermal−isobaric ensemble with the AMBER RNA force field.[79] Simulations used a cutoff of 8 Å and a timestep of 2.5 fs. The models employed an improved Berendsen Thermostat[80] and a particle mesh Ewald.[81] Simulation conditions were conducted with periodic boundaries at 0.9% NaCl (w/v), pH 7.4, 298 K, and at atmospheric pressure. Water was filled to a density of 0.997 g/mL and was modeled with a TIP3P equivalent.

The tension probes were constructed in pieces using existing experimentally verified structures. The 20 nt duplex arms were created through in silico mutation of an NMR-acquired structure of a 21 bp DNA duplex (PDB: 2JYK).[82] The hairpin portion was based off an NMR-acquired structure of a 27 nt AT-rich hairpin with a 3T loop (PDB: 1JVE) and was modified in silico.[83] The models were relaxed in an incremental fashion to maintain a reasonable structure and then were ligated with the 3T spacers flanking the stem−loop. The final probe structure with the spacers was then produced by stepwise relaxation. To produce the final probe lacking spacers, the 3T loops were excised from the standard hairpin strand and the structure again was relaxed in a stepwise fashion. 5T overhangs were added in YASARA to both of these structures, and their addition was followed by a stepwise relaxation to produce D probes containing a 5T overhang at the 3′ terminus of the donor strand.

For each simulation frame, the distances between the C1 atoms of the ends of the duplexes facing the hairpin were calculated. The distances between the nucleobase hydrogen bond donors and their acceptor partners were calculated for each nucleobase surrounding the duplex/hairpin junction and were averaged to produce a distance for each nucleobase. Molecular dynamics simulations were conducted in triplicate. To minimize the role of starting conformations on simulation outcome, starting structures for the replicate simulations were obtained through energy minimization of the structure captured at 3.3 ns of the previous replicate; the random number seed was also changed, and the simulation rerun under otherwise identical conditions.

To supplement these data, base pair probabilities for the hairpin probes were calculated using the freely available NUPACK package[84] with dangle treatment applied. Probes were computationally hybridized at 0.5 μM (1×) with 10% excess of the donor strand sequence. Simulations were analyzed at 25 °C in 137 mM Na^+, which corresponded to 1× PBS. These conditions matched the conditions used to hybridize DNA prior to SBL functionalization.

The distances between biotin groups in the dual-biotin modification and between biotin binding sites in streptavidin were determined from 3D structures using PyMol (version 2.3.5). Biotin−streptavidin interaction was modeled using a previously published crystal structure (MMDB 92935)[85] with all four tetramer subunits displayed. The simplified dual-biotin linker structure was modeled in WebMO (version 19.0.009e) and was input into PyMol. The biotin−biotin distance was calculated as the distance between nitrogen atoms.

UV−Vis Spectroscopy. Tension probes were hybridized at 2.5 μM and concentrated to ∼10 μM prior to measuring on a Thermo Scientific Nanodrop 2000c spectrophotometer with a 0.1 cm pathlength. The closed samples were rehybridized, concentrated, and measured with the complementary sequence to obtain the open spectra.

Microscopy. Epifluorescence imaging was carried out using the Nikon Elements 4.40.00 or 4.13.05 software and a 1.49 NA CFI Apo 100× objective on a Nikon Eclipse Ti microscope. For probe characterization, all imaging was performed with an identical setup. For dual-biotin experiments, to account for cube differences on separate microscopes, all data were normalized. Fluorescence lifetime imaging was performed on a Nikon Ti Eclipse Inverted confocal microscope with a Plan Apo Lambda 60×/1.40 Oil objective, Nikon Elements 4.40.00, perfect focus, and a C2 laser launch. The microscope was updated with a Picoquant laser scanning microscope time-correlated photon counting (TCSPC) Upgrade with SymPhoTime 64 2.1.3813 software. The FLIM samples were excited with a 20 MHz pulsed 514 or 485 nm laser, and the images were collected at 0.5 frames/s. The samples were imaged at 20 MHz with a photon count rate of ∼5% of the laser pulse rate, except for the Cy3B/BHQ1 probes that were limited by sample brightness, and the A_A488/Cy3B− probes, which were collected at a lower count rate to minimize bleaching. For each class of probes, the photon count rate was maintained for the open and closed samples. Light was filtered using a long-pass laser beamsplitter (H560 LPXR or H488 LPXR, Analysentechnik) and a 582/75 bandpass filter (F37-582, Semrock) or 525/35 bandpass. Laser light that was reflected by the dichroic was blocked from an additional detector using a 690/35 bandpass filter. Surface characterization was performed with the pinhole fully opened. For cellular imaging, the A_Cy3B/BHQ1 samples were imaged with an open pinhole to maximize light collection; the S_Cy3B/BHQ1 and A_A488/BHQ1 samples were imaged with the pinhole optimized to 1.2 airy units. Imaging was conducted in perfect focus mode.

https://dx.doi.org/10.1021/acsami.0c09774
ACS Appl. Mater. Interfaces XXXX, XXX, XXX−XXX

Cell Culture. The NIH-3T3 fibroblasts were cultured in Dulbecco's modification of Eagle's medium (DMEM) (B003K32, Corning). Media contained 10% fetal bovine serum (USDAFBS, MidSci), 2.5 mM L-glutamine (G8540, Millipore-Sigma), and 1× penicillin−streptomycin (97063-708, VWR). The cells were incubated at 37 °C in 5% CO_2. The cells were authenticated by IDEXX Bioresearch. Note that while these surpassed the criteria for cell line validation,[86] they did show small genetic deviation. Nevertheless, we find these cells to be a robust podosome model.

Analysis and Statistics. Fluorescence lifetime decay traces were fit using reconvolution in SymPhoTime 64 according to the equation

$$I(t) = \sum_{n=1}^{m} A_n \, e^{-t/\tau_n} \tag{2}$$

Goodness of fit was evaluated by the χ^2 parameter. Fits were performed with an automated IRF. If the automated IRF was significantly elongated, the start of the decay curve was truncated, to remove empty bins and restore the expected IRF. All curve fits had $\chi^2 < 2$. The curves were fit with the minimum number of lifetimes to reduce sinusoidal residuals while minimizing $\chi^2 < 2$. If additional lifetime components only corrected deviations near the IRF region, the lower lifetime fit was selected. All open probes were fit to monoexponential decays. The closed probes were fit to bi- or triexponential decays. Lifetime fits were performed on regions-of-interest (ROIs) containing ~10^3−10^4 photons in the decay peak. We found that this intensity was optimal to minimize the contribution of detector nonlinearities, which had prevented curve fitting of our MT-FLIM data in its original report.[16] Curve-fit data were used to calculate the intensity and amplitude-weighted average fluorescence lifetimes in the picoquant software according to the following equations

$$\tau_{\text{Av Int}} = \frac{\sum A_n \tau_n^2}{\sum A_n \tau_n} \tag{3}$$

$$\tau_{\text{Av Amp}} = \frac{\sum A_n \tau_n}{\sum A_n} \tag{4}$$

The amplitude average lifetime was used to calculate the lifetime-based QE

$$E = 100 \times \left(1 - \frac{\tau_{\text{Av Amp,Closed}}}{\tau_{\text{Av Amp,Open}}}\right) \tag{5}$$

Note that this value poorly agreed with the QE calculated from epifluorescence images, which can be expected for a system with mixed static quenching and probe dynamics.[49,87] Statistical analysis and plotting were performed in MATLAB. ROIs were also used to generate $\tau_{\text{Av FAST}}$, which represent the center-of-mass fluorescence lifetime weighted by the number of events. To obtain the average fluorescence lifetime from these data, histograms were fit to a curve in MATLAB according to the equation

$$y = \sum_{n=1}^{2} a_n \, e^{-((x-b_n)/c_n)^2} \tag{6}$$

b_1 was used for the average fluorescence lifetime and c_1 reflected the peak width. Data in Figure 6 were fit a mono- instead of a bi-exponential equation. Fluorescence intensity data was processed in MATLAB. The aggregates and holes in the SLB were omitted by standard deviation-based thresholding, and the average fluorescence intensity was calculated from the central region of the SLB. The QE was calculated by the following equation

$$E = 100 \times \left(1 - \frac{I,\ \text{Closed}}{I,\ \text{Open}}\right) \tag{7}$$

For single versus dual-biotin analysis, the quenching efficiency was determined from the linear regression curve fit of intensity data. Absorbance data was processed in MATLAB. The curves were background-corrected using the baseline absorbance between 720 and 750 nm and were normalized to the absorption maximum. The donor or acceptor-labeled probes were normalized to the corresponding label. The absorption peaks of the average, normalized samples were identified using PeakFinder version 6 with pseudo-Gaussian smoothing. To account for BHQ1's broad absorption, BHQ1 only samples, data were averaged across 10 nm before peak detection, and detected peaks had a minimum first derivative of 0.00005. For all other samples, the peaks with a minimum first derivative of 0.003 were detected, and data were not averaged. The minimum peak intensity was set to avoid noise detection. The computed FRET spectra were calculated from the extinction coefficient-weighted sum of the donor and acceptor probe spectra.

Cell image analysis was performed as illustrated in Figures S12−S14. Following initial masking of podosomes, an equal number of pixels were randomly selected from the SLB background for quantitative analysis on scatter plots and in histograms. The FAST FLIM average lifetime per pixel was used to calculate statistics on the masked regions.

At least three independent experiments were performed. For cell studies, independent experiments were defined by a flask or well of cells. For cell-free studies, independent experiments were defined by a surface or sample, and at least three measurements were performed. Statistical tests and outlier testing were performed, as described in the figure captions.

Estimation of $F_{1/2}$. For cell experiments in this manuscript, $F_{1/2}$ is defined by the previously experimentally calibrated value of 4.7 pN.[15,16] However, to estimate the impact of fraying in the discussion section, $F_{1/2}$ was calculated as the sum of the free energy of unfolding the hairpin, ΔG_{Unfold}, and the free energy of stretching single-stranded DNA in the hairpin, $\Delta G_{\text{Stretch}}$

$$F_{1/2} = (\Delta G_{\text{Unfold}} + \Delta G_{\text{Stretch}})/\Delta X \tag{8}$$

Here, ΔG_{Unfold} is defined as $-\Delta G_{\text{Fold}}$, where ΔG_{Fold} is determined with Integrated DNA Technologies' OligoAnalyzer Tool using the hairpin mode. $\Delta G_{\text{Stretch}}$ is derived from the worm-like chain model for polymer extension

$$\Delta G_{\text{Stretch}} = \frac{k_B T}{L_p} \frac{L_0}{4(1 - \Delta X/L_0)} [3(\Delta X/L_0)^2 - 2(\Delta X/L_0)^3] \tag{9}$$

In this equation, k_B is the Boltzmann constant, T is the temperature, and L_p is the persistence length of single-stranded DNA. ΔX is the change in distance upon hairpin opening and L_0 is the contour length of the single-stranded hairpin sequence. Here, $\Delta X = 10^{-9}$ [$0.44(n - 1) - 2$], with n equal to the number of bases in the DNA hairpin. We subtract 2 nm for the initial duplex width. $L_0 = (0.63 \times 10^{-9})n$. To approximate the effect of fraying on a DNA hairpin's $F_{1/2}$, we considered a truncated "effective" hairpin sequence (Table S8). The calculations were performed at 298 K in 137 mM NaCl, which corresponds to 1× PBS. A more extensive discussion of this model can be found in Zhang et al.[15] and Woodside et al.[12]

■ ASSOCIATED CONTENT

Supporting Information

The Supporting Information is available free of charge at https://pubs.acs.org/doi/10.1021/acsami.0c09774.

Probe sequences and characterization, supplementary bilayer and probe analysis, representative TCSPC curve fits and residuals, and graphical summaries of cellular analysis (PDF)

■ AUTHOR INFORMATION

Corresponding Author

Khalid Salaita − *Wallace H. Coulter Department of Biomedical Engineering at Georgia Institute of Technology and Emory University, Atlanta, Georgia 30322, United*

https://dx.doi.org/10.1021/acsami.0c09774
ACS Appl. Mater. Interfaces XXXX, XXX, XXX−XXX

States; Department of Chemistry, Emory University, Atlanta, Georgia 30322, United States; orcid.org/0000-0003-4138-3477; Email: k.salaita@emory.edu

Authors

Roxanne Glazier − *Wallace H. Coulter Department of Biomedical Engineering at Georgia Institute of Technology and Emory University, Atlanta, Georgia 30322, United States;* orcid.org/0000-0002-2270-2551

Pushkar Shinde − *Department of Chemistry, Emory University, Atlanta, Georgia 30322, United States;* orcid.org/0000-0002-8086-4321

Hiroaki Ogasawara − *Department of Chemistry, Emory University, Atlanta, Georgia 30322, United States;* orcid.org/0000-0001-8462-562X

Complete contact information is available at: https://pubs.acs.org/10.1021/acsami.0c09774

Author Contributions

R.G. and K.S. designed the experiments. R.G. performed and analyzed the imaging and spectroscopy data. H.O. contributed the mass spectrometry, PyMOL modeling, and analysis. P.S. performed the MD simulation and analysis. R.G. and K.S. wrote and revised the manuscript. H.O. and P.S. contributed to the manuscript. All authors have approved the final version of the manuscript.

Funding

This work was funded by the National Institute of Health (R01-GM131099 and R01-GM124472) and the National Science Foundation (CAREER award 1350829). This material is also based upon work supported by the National Science Foundation Graduate Research Fellowship Program under Grant no. DGE-1444932 (R.G.). H.O. acknowledges the Naito Foundation and the Uehara Memorial Foundation for the research support.

Notes

The authors declare no competing financial interest.

ABBREVIATIONS

A, adjacent
A488, Alexa Fluor 488
bp, base pair
BHQ1, black hole quencher 1
cRGD, cyclic arginine-glycine-aspartate
D, dangling
DET, dexter energy transfer
ECM, extracellular matrix
FLIM, fluorescence lifetime imaging microscopy
IRF, instrument response function
nt, nucleotide
MT-FLIM, molecular tension-fluorescence lifetime imaging microscopy
MTFM, molecular tension fluorescence microscopy
nN, nanonewton
pN, piconewton
S, separated
SLB, supported lipid bilayer
SNR, signal-to-noise ratio
TCSPC, time-correlated single-photon counting
TFM, traction force microscopy
TWJ, three-way junction
QE, quenching efficiency

REFERENCES

(1) Martino, F.; Perestrelo, A. R.; Vinarsky, V.; Pagliari, S.; Forte, G. Cellular Mechanotransduction: From Tension to Function. *Front. Physiol.* **2018**, *9*, No. 824.
(2) Grashoff, C.; Hoffman, B. D.; Brenner, M. D.; Zhou, R.; Parsons, M.; Yang, M. T.; McLean, M. A.; Sligar, S. G.; Chen, C. S.; Ha, T.; Schwartz, M. A. Measuring Mechanical Tension across Vinculin Reveals Regulation of Focal Adhesion Dynamics. *Nature* **2010**, *466*, 263−266.
(3) Lam, W. A.; Chaudhuri, O.; Crow, A.; Webster, K. D.; Li, T.-D.; Kita, A.; Huang, J.; Fletcher, D. A. Mechanics and Contraction Dynamics of Single Platelets and Implications for Clot Stiffening. *Nat. Mater.* **2011**, *10*, 61−66.
(4) Zhang, Y.; Qiu, Y.; Blanchard, A. T.; Chang, Y.; Brockman, J. M.; Ma, V. P.; Lam, W. A.; Salaita, K. Platelet Integrins Exhibit Anisotropic Mechanosensing and Harness Piconewton Forces to Mediate Platelet Aggregation. *Proc. Natl. Acad. Sci. U.S.A.* **2018**, *115*, 325−330.
(5) Liu, Y.; Blanchfield, L.; Ma, V. P.; Andargachew, R.; Galior, K.; Liu, Z.; Evavold, B.; Salaita, K. DNA-Based Nanoparticle Tension Sensors Reveal That T-Cell Receptors Transmit Defined Pn Forces to Their Antigens for Enhanced Fidelity. *Proc. Natl. Acad. Sci. U.S.A.* **2016**, *113*, 5610−5615.
(6) Upadhyaya, A. Mechanosensing in the Immune Response. *Semin. Cell Dev. Biol.* **2017**, *71*, 137−145.
(7) Style, R. W.; Boltyanskiy, R.; German, G. K.; Hyland, C.; MacMinn, C. W.; Mertz, A. F.; Wilen, L. A.; Xu, Y.; Dufresne, E. R. Traction Force Microscopy in Physics and Biology. *Soft Matter* **2014**, *10*, 4047−4055.
(8) Ricart, B. G.; Yang, M. T.; Hunter, C. A.; Chen, C. S.; Hammer, D. A. Measuring Traction Forces of Motile Dendritic Cells on Micropost Arrays. *Biophys. J.* **2011**, *101*, 2620−2628.
(9) Stabley, D. R.; Jurchenko, C.; Marshall, S. S.; Salaita, K. S. Visualizing Mechanical Tension across Membrane Receptors with a Fluorescent Sensor. *Nat. Methods* **2012**, *9*, 64−67.
(10) Blanchard, A. T.; Salaita, K. Emerging Uses of DNA Mechanical Devices. *Science* **2019**, *365*, 1080−1081.
(11) Liu, Y.; Galior, K.; Ma, V. P.; Salaita, K. Molecular Tension Probes for Imaging Forces at the Cell Surface. *Acc. Chem. Res.* **2017**, *50*, 2915−2924.
(12) Woodside, M. T.; Behnke-Parks, W. M.; Larizadeh, K.; Travers, K.; Herschlag, D.; Block, S. M. Nanomechanical Measurements of the Sequence-Dependent Folding Landscapes of Single Nucleic Acid Hairpins. *Proc. Natl. Acad. Sci. U.S.A.* **2006**, *103*, 6190.
(13) Ma, R.; Kellner, A. V.; Ma, V. P.-Y.; Su, H.; Deal, B. R.; Brockman, J. M.; Salaita, K. DNA Probes That Store Mechanical Information Reveal Transient Piconewton Forces Applied by T Cells. *Proc. Natl. Acad. Sci. U.S.A.* **2019**, 16949.
(14) Nowosad, C. R.; Spillane, K. M.; Tolar, P. Germinal Center B Cells Recognize Antigen through a Specialized Immune Synapse Architecture. *Nat. Immunol.* **2016**, *17*, 870−877.
(15) Zhang, Y.; Ge, C.; Zhu, C.; Salaita, K. DNA-Based Digital Tension Probes Reveal Integrin Forces During Early Cell Adhesion. *Nat. Commun.* **2014**, *5*, No. 5167.
(16) Glazier, R.; Brockman, J. M.; Bartle, E.; Mattheyses, A. L.; Destaing, O.; Salaita, K. DNA Mechanotechnology Reveals That Integrin Receptors Apply Pn Forces in Podosomes on Fluid Substrates. *Nat. Commun.* **2019**, *10*, No. 4507.
(17) Galior, K.; Liu, Y.; Yehl, K.; Vivek, S.; Salaita, K. Titin-Based Nanoparticle Tension Sensors Map High-Magnitude Integrin Forces within Focal Adhesions. *Nano Lett.* **2016**, *16*, 341−348.
(18) Liu, Y.; Medda, R.; Liu, Z.; Galior, K.; Yehl, K.; Spatz, J. P.; Cavalcanti-Adam, E. A.; Salaita, K. Nanoparticle Tension Probes Patterned at the Nanoscale: Impact of Integrin Clustering on Force Transmission. *Nano Lett.* **2014**, *14*, 5539−5546.
(19) Blakely, B. L.; Dumelin, C. E.; Trappmann, B.; McGregor, L. M.; Choi, C. K.; Anthony, P. C.; Duesterberg, V. K.; Baker, B. M.; Block, S. M.; Liu, D. R.; Chen, C. S. A DNA-Based Molecular Probe

for Optically Reporting Cellular Traction Forces. *Nat. Methods* **2014**, *11*, 1229−1232.
(20) Wan, Z.; Chen, X.; Chen, H.; Ji, Q.; Chen, Y.; Wang, J.; Cao, Y.; Wang, F.; Lou, J.; Tang, Z.; Liu, W. The Activation of Igm- or Isotype-Switched Igg- and Ige-Bcr Exhibits Distinct Mechanical Force Sensitivity and Threshold. *eLife* **2015**, *4*, No. e06925.
(21) Brockman, J. M.; Blanchard, A. T.; Pui-Yan, V. M.; Derricotte, W. D.; Zhang, Y.; Fay, M. E.; Lam, W. A.; Evangelista, F. A.; Mattheyses, A. L.; Salaita, K. Mapping the 3d Orientation of Piconewton Integrin Traction Forces. *Nat. Methods* **2018**, *15*, 115−118.
(22) Glazier, R.; Salaita, K. Supported Lipid Bilayer Platforms to Probe Cell Mechanobiology. *Biochim. Biophys. Acta, Biomembr.* **2017**, *1859*, 1465−1482.
(23) Salaita, K.; Nair, P. M.; Petit, R. S.; Neve, R. M.; Das, D.; Gray, J. W.; Groves, J. T. Restriction of Receptor Movement Alters Cellular Response: Physical Force Sensing by Epha2. *Science* **2010**, *327*, 1380−1385.
(24) Narui, Y.; Salaita, K. Membrane Tethered Delta Activates Notch and Reveals a Role for Spatio-Mechanical Regulation of the Signaling Pathway. *Biophys. J.* **2013**, *105*, 2655−2665.
(25) Chaudhuri, O.; Gu, L.; Klumpers, D.; Darnell, M.; Bencherif, S. A.; Weaver, J. C.; Huebsch, N.; Lee, H.-P.; Lippens, E.; Duda, G. N.; Mooney, D. J. Hydrogels with Tunable Stress Relaxation Regulate Stem Cell Fate and Activity. *Nat. Mater.* **2016**, *15*, 326−334.
(26) Ma, V. P.-Y.; Liu, Y.; Blanchfield, L.; Su, H.; Evavold, B. D.; Salaita, K. Ratiometric Tension Probes for Mapping Receptor Forces and Clustering at Intermembrane Junctions. *Nano Lett.* **2016**, *16*, 4552−4559.
(27) Zhao, B.; Li, N.; Xie, T.; Liang, C.; Bagheri, Y.; Sun, Y.; You, M. Quantifying Tensile Forces at Cell−Cell Junctions with a DNA-Based Fluorescent Probe. *bioRxiv* **2020**, 1−30.
(28) Merindol, R.; Delechiave, G.; Heinen, L.; Catalani, L. H.; Walther, A. Modular Design of Programmable Mechanofluorescent DNA Hydrogels. *Nat. Commun.* **2019**, *10*, No. 528.
(29) Kilin, V.; Glushonkov, O.; Herdly, L.; Klymchenko, A.; Richert, L.; Mely, Y. Fluorescence Lifetime Imaging of Membrane Lipid Order with a Ratiometric Fluorescent Probe. *Biophys. J.* **2015**, *108*, 2521−2531.
(30) Wang, Y.-L. Noise-Induced Systematic Errors in Ratio Imaging: Serious Artefacts and Correction with Multi-Resolution Denoising. *J. Microsc.* **2007**, *228*, 123−131.
(31) Iqbal, A.; Arslan, S.; Okumus, B.; Wilson, T. J.; Giraud, G.; Norman, D. G.; Ha, T.; Lilley, D. M. Orientation Dependence in Fluorescent Energy Transfer between Cy3 and Cy5 Terminally Attached to Double-Stranded Nucleic Acids. *Proc. Natl. Acad. Sci. U.S.A.* **2008**, *105*, 11176−11181.
(32) Ranjit, S.; Gurunathan, K.; Levitus, M. Photophysics of Backbone Fluorescent DNA Modifications: Reducing Uncertainties in Fret. *J. Phys. Chem. B* **2009**, *113*, 7861−7866.
(33) Di Fiori, N.; Meller, A. The Effect of Dye-Dye Interactions on the Spatial Resolution of Single-Molecule Fret Measurements in Nucleic Acids. *Biophys. J.* **2010**, *98*, 2265−2272.
(34) Wang, L.; Gaigalas, A. K.; Blasic, J.; Holden, M. J.; Gallagher, D. T.; Pires, R. Fluorescence Resonance Energy Transfer between Donor-Acceptor Pair on Two Oligonucleotides Hybridized Adjacently to DNA Template. *Biopolymers* **2003**, *72*, 401−412.
(35) Jurchenko, C.; Salaita, K. S. Lighting up the Force: Investigating Mechanisms of Mechanotransduction Using Fluorescent Tension Probes. *Mol. Cell. Biol.* **2015**, *35*, 2570−2582.
(36) Algar, W. R.; Hildebrandt, N.; Vogel, S. S.; Medintz, I. L. Fret as a Biomolecular Research Tool - Understanding Its Potential While Avoiding Pitfalls. *Nat Methods* **2019**, *16*, 815−829.
(37) Johansson, M. K. Choosing Reporter−Quencher Pairs for Efficient Quenching through Formation of Intramolecular Dimers. In *Fluorescent Energy Transfer Nucleic Acid Probes: Designs and Protocols*; Didenko, V. V., Ed.; Humana Press: Totowa, NJ, 2006; pp 17−29.
(38) Marras, S. A. E.; Kramer, F. R.; Tyagi, S. Efficiencies of Fluorescence Resonance Energy Transfer and Contact-Mediated Quenching in Oligonucleotide Probes. *Nucleic Acids Res.* **2002**, *30*, No. e122.
(39) Ko, J.; Oh, J.; Ahmed, M. S.; Carlson, J. C. T.; Weissleder, R. Ultra-Fast Cycling for Multiplexed Cellular Fluorescence Imaging. *Angew. Chem., Int. Ed.* **2020**, 6839.
(40) Cooper, M.; Ebner, A.; Briggs, M.; Burrows, M.; Gardner, N.; Richardson, R.; West, R. Cy3b: Improving the Performance of Cyanine Dyes. *J. Fluoresc.* **2004**, *14*, 145−150.
(41) Kasha, M. Energy Transfer Mechanisms and the Molecular Exciton Model for Molecular Aggregates. *Radiat. Res.* **1963**, *20*, 55−70.
(42) Valdes-Aguilera, O.; Neckers, D. C. Aggregation Phenomena in Xanthene Dyes. *Acc. Chem. Res.* **1989**, *22*, 171−177.
(43) Woźniak, A. K.; Schröder, G. F.; Grubmüller, H.; Seidel, C. A. M.; Oesterhelt, F. Single-Molecule Fret Measures Bends and Kinks in DNA. *Proc. Natl. Acad. Sci. U.S.A.* **2008**, *105*, 18337.
(44) Leontis, N.; Kwok, W.; Newman, J. Stability and Structure of Three-Way DNA Junctions Containing Unpaired Nucleotides. *Nucleic Acids Res.* **1991**, *19*, 759−766.
(45) Leontis, N. B.; Hills, M. T.; Piotto, M.; Ouporov, I. V.; Malhotra, A.; Gorenstein, D. G. Helical Stacking in DNA Three-Way Junctions Containing Two Unpaired Pyrimidines: Proton NMR Studies. *Biophys. J.* **1995**, *68*, 251−265.
(46) Welch, J. B.; Duckett, D. R.; Lilley, D. M. Structures of Bulged Three-Way DNA Junctions. *Nucleic Acids Res.* **1993**, *21*, 4548−4555.
(47) Wu, Z.; Ono, A.; Kainosho, M.; Bax, A. H···N Hydrogen Bond Lengths in Double Stranded DNA from Internucleotide Dipolar Couplings. *J. Biomol. NMR* **2001**, *19*, 361−365.
(48) Speiser, S. Photophysics and Mechanisms of Intramolecular Electronic Energy Transfer in Bichromophoric Molecular Systems: Solution and Supersonic Jet Studies. *Chem. Rev.* **1996**, *96*, 1953−1976.
(49) Sillen, A.; Engelborghs, Y. The Correct Use of "Average" Fluorescence Parameters. *Photochem. Photobiol.* **1998**, *67*, 475−486.
(50) Dubacheva, G. V.; Araya-Callis, C.; Geert Volbeda, A.; Fairhead, M.; Codée, J.; Howarth, M.; Richter, R. P. Controlling Multivalent Binding through Surface Chemistry: Model Study on Streptavidin. *J. Am. Chem. Soc.* **2017**, *139*, 4157−4167.
(51) Fairhead, M.; Krndija, D.; Lowe, E. D.; Howarth, M. Plug-and-Play Pairing Via Defined Divalent Streptavidins. *J. Mol. Biol.* **2014**, *426*, 199−214.
(52) Labernadie, A.; Bouissou, A.; Delobelle, P.; Balor, S.; Voituriez, R.; Proag, A.; Fourquaux, I.; Thibault, C.; Vieu, C.; Poincloux, R.; Charrière, G. M.; Maridonneau-Parini, I. Protrusion Force Microscopy Reveals Oscillatory Force Generation and Mechanosensing Activity of Human Macrophage Podosomes. *Nat. Commun.* **2014**, *5*, No. 5343.
(53) van den Dries, K.; Bolomini-Vittori, M.; Cambi, A. Spatiotemporal Organization and Mechanosensory Function of Podosomes. *Cell Adhes. Migr.* **2014**, *8*, 268−272.
(54) van den Dries, K.; Schwartz, S. L.; Byars, J.; Meddens, M. B.; Bolomini-Vittori, M.; Lidke, D. S.; Figdor, C. G.; Lidke, K. A.; Cambi, A. Dual-Color Superresolution Microscopy Reveals Nanoscale Organization of Mechanosensory Podosomes. *Mol. Biol. Cell* **2013**, *24*, 2112−2123.
(55) Yu, C. H.; Rafiq, N. B.; Krishnasamy, A.; Hartman, K. L.; Jones, G. E.; Bershadsky, A. D.; Sheetz, M. P. Integrin-Matrix Clusters Form Podosome-Like Adhesions in the Absence of Traction Forces. *Cell Rep.* **2013**, *5*, 1456−1468.
(56) Rafiq, N. B. M.; Lieu, Z. Z.; Jiang, T.; Yu, C.-h.; Matsudaira, P.; Jones, G. E.; Bershadsky, A. D. Podosome Assembly Is Controlled by the Gtpase Arf1 and Its Nucleotide Exchange Factor Arno. *J. Cell Biol.* **2017**, *216*, 181−197.
(57) Cao, F.; Zhou, Y.; Liu, X.; Yu, C.-h. Podosome Formation Promotes Plasma Membrane Invagination and Integrin-B3 Endocytosis on a Viscous Rgd-Membrane. *Commun. Biol.* **2020**, *3*, No. 117.
(58) Melinger, J. S.; Khachatrian, A.; Ancona, M. G.; Buckhout-White, S.; Goldman, E. R.; Spillmann, C. M.; Medintz, I. L.;

https://dx.doi.org/10.1021/acsami.0c09774
ACS Appl. Mater. Interfaces XXXX, XXX, XXX−XXX

Cunningham, P. D. Fret from Multiple Pathways in Fluorophore-Labeled DNA. *ACS Photonics* **2016**, *3*, 659−669.
(59) Dietrich, A.; Buschmann, V.; Muller, C.; Sauer, M. Fluorescence Resonance Energy Transfer (Fret) and Competing Processes in Donor-Acceptor Substituted DNA Strands: A Comparative Study of Ensemble and Single-Molecule Data. *J. Biotechnol.* **2002**, *82*, 211−231.
(60) Qu, P.; Chen, X.; Zhou, X.; Li, X.; Zhao, X. Fluorescence Quenching of TMR by Guanosine in Oligonucleotides. *Sci. China, Ser. B: Chem.* **2009**, *52*, 1653−1659.
(61) Lindhoud, S.; Westphal, A. H.; Visser, A. J. W. G.; Borst, J. W.; van Mierlo, C. P. M. Fluorescence of Alexa Fluor Dye Tracks Protein Folding. *PLoS One* **2012**, *7*, No. e46838.
(62) von Hippel, P. H.; Johnson, N. P.; Marcus, A. H. Fifty Years of DNA "Breathing": Reflections on Old and New Approaches. *Biopolymers* **2013**, *99*, 923−954.
(63) Hughes, L. D.; Rawle, R. J.; Boxer, S. G. Choose Your Label Wisely: Water-Soluble Fluorophores Often Interact with Lipid Bilayers. *PLoS One* **2014**, *9*, No. e87649.
(64) Fišerová, E.; Kubala, M. Mean Fluorescence Lifetime and Its Error. *J. Lumin.* **2012**, *132*, 2059−2064.
(65) Szabó, Á.; Szendi-Szatmári, T.; Ujlaky-Nagy, L.; Rádi, I.; Vereb, G.; Szöllősi, J.; Nagy, P. The Effect of Fluorophore Conjugation on Antibody Affinity and the Photophysical Properties of Dyes. *Biophys. J.* **2018**, *114*, 688−700.
(66) You, Y.; Tataurov, A. V.; Owczarzy, R. Measuring Thermodynamic Details of DNA Hybridization Using Fluorescence. *Biopolymers* **2011**, *95*, 472−486.
(67) Kretschy, N.; Sack, M.; Somoza, M. M. Sequence-Dependent Fluorescence of Cy3- and Cy5-Labeled Double-Stranded DNA. *Bioconjugate Chem.* **2016**, *27*, 840−848.
(68) Noble, J. E.; Wang, L.; Cole, K. D.; Gaigalas, A. K. The Effect of Overhanging Nucleotides on Fluorescence Properties of Hybridising Oligonucleotides Labelled with Alexa-488 and Fam Fluorophores. *Biophys. Chem.* **2005**, *113*, 255−263.
(69) Smoligovets, A.; Smith, A.; Wu, H.-J.; Petit, R.; Groves, J. Characterization of Dynamic Actin Associations with T-Cell Receptor Microclusters in Primary T Cells. *J. Cell Sci.* **2012**, *125*, 735−742.
(70) Lakowicz, J. R. *Principles of Fluorescence Spectroscopy*, 2nd ed.; Kluwer Academic/Plenum: New York, 1999.
(71) Melavanki, R. M.; Kusanur, R. A.; Kadadevaramath, J. S.; Kulkarni, M. V. Effect of Solvent Polarity on the Fluorescence Quenching of Biologically Active 5bamc by Aniline in Binary Solvent Mixtures. *J. Fluoresc.* **2010**, *20*, 1175−1180.
(72) Roy, R.; Hohng, S.; Ha, T. A Practical Guide to Single-Molecule Fret. *Nat. Methods* **2008**, *5*, 507−516.
(73) Pan, K.; Boulais, E.; Yang, L.; Bathe, M. Structure-Based Model for Light-Harvesting Properties of Nucleic Acid Nanostructures. *Nucleic Acids Res.* **2014**, *42*, 2159−2170.
(74) Buckhout-White, S.; Spillmann, C. M.; Algar, W. R.; Khachatrian, A.; Melinger, J. S.; Goldman, E. R.; Ancona, M. G.; Medintz, I. L. Assembling Programmable Fret-Based Photonic Networks Using Designer DNA Scaffolds. *Nat. Commun.* **2014**, *5*, No. 5615.
(75) Pehlivan, Z. S.; Torabfam, M.; Kurt, H.; Ow-Yang, C.; Hildebrandt, N.; Yüce, M. Aptamer and Nanomaterial Based Fret Biosensors: A Review on Recent Advances (2014-2019). *Mikrochim. Acta* **2019**, *186*, No. 563.
(76) Krieger, E.; Vriend, G. New Ways to Boost Molecular Dynamics Simulations. *J. Comput. Chem.* **2015**, *36*, 996−1007.
(77) de Groot, B. L.; van Aalten, D. M. F.; Scheek, R. M.; Amadei, A.; Vriend, G.; Berendsen, H. J. C. Prediction of Protein Conformational Freedom from Distance Constraints. *Proteins: Struct., Funct., Bioinf.* **1997**, *29*, 240−251.
(78) Krieger, E.; Nielsen, J. E.; Spronk, C. A. E. M.; Vriend, G. Fast Empirical Pka Prediction by Ewald Summation. *J. Mol. Graphics Modell.* **2006**, *25*, 481−486.
(79) Pettersen, E. F.; Goddard, T. D.; Huang, C. C.; Couch, G. S.; Greenblatt, D. M.; Meng, E. C.; Ferrin, T. E. Ucsf Chimera–a Visualization System for Exploratory Research and Analysis. *J. Comput. Chem.* **2004**, *25*, 1605−1612.
(80) Krieger, E.; Darden, T.; Nabuurs, S. B.; Finkelstein, A.; Vriend, G. Making Optimal Use of Empirical Energy Functions: Force-Field Parameterization in Crystal Space. *Proteins: Struct., Funct., Bioinf.* **2004**, *57*, 678−683.
(81) Essmann, U.; Perera, L.; Berkowitz, M. L.; Darden, T.; Lee, H.; Pedersen, L. G. A Smooth Particle Mesh Ewald Method. *J. Chem. Phys.* **1995**, *103*, 8577−8593.
(82) Masliah, G.; René, B.; Zargarian, L.; Fermandjian, S.; Mauffret, O. Identification of Intrinsic Dynamics in a DNA Sequence Preferentially Cleaved by Topoisomerase Ii Enzyme. *J. Mol. Biol.* **2008**, *381*, 692−706.
(83) Ulyanov, N. B.; Bauer, W. R.; James, T. L. High-Resolution NMR Structure of an at-Rich DNA Sequence. *J. Biomol. NMR* **2002**, *22*, 265−280.
(84) Zadeh, J. N.; Steenberg, C. D.; Bois, J. S.; Wolfe, B. R.; Pierce, M. B.; Khan, A. R.; Dirks, R. M.; Pierce, N. A. Nupack: Analysis and Design of Nucleic Acid Systems. *J. Comput. Chem.* **2011**, *32*, 170−173.
(85) Le Trong, I.; Wang, Z.; Hyre, D. E.; Lybrand, T. P.; Stayton, P. S.; Stenkamp, R. E. Streptavidin and Its Biotin Complex at Atomic Resolution. *Acta Crystallogr., Sect. D: Biol. Crystallogr.* **2011**, *67*, 813−821.
(86) Reid, Y.; Storts, D.; Riss, T.; Minor, L. In *Assay Guidance Manual: Authentication of Human Cell Lines by STR DNA Profiling Analysis*; Markossian, S. et al., Ed.; Eli Lily & Company and National Center for Advancing Translational Sciences: Bethesda, Maryland, 2013. https://www.ncbi.nlm.nih.gov/books/NBK144066/.
(87) Gopich, I. V.; Szabo, A. Theory of the Energy Transfer Efficiency and Fluorescence Lifetime Distribution in Single-Molecule Fret. *Proc. Natl. Acad. Sci. U.S.A.* **2012**, *109*, 7747−7752.

https://dx.doi.org/10.1021/acsami.0c09774
ACS Appl. Mater. Interfaces XXXX, XXX, XXX−XXX